

# Experimental study of the initial stages of wind waves' spatial evolution

DAN LIBERZON<sup>†</sup> AND LEV SHEMER

Tel Aviv University, School of Mechanical Engineering, Tel Aviv 69978, Israel

(Received 30 August 2010; revised 4 May 2011; accepted 5 May 2011;  
first published online 24 June 2011)

Despite a significant progress and numerous publications over the last few decades a comprehensive understanding of the process of waves' excitation by wind still has not been achieved. The main goal of the present work was to provide as comprehensive as possible set of experimental data that can be quantitatively compared with theoretical models. Measurements at various air flow rates and at numerous fetches were carried out in a small scale, closed-loop, 5 m long wind wave flume. Mean airflow velocity and fluctuations of the static pressure were measured at 38 vertical locations above the mean water surface simultaneously with determination of instantaneous water surface elevations by wave gauges. Instantaneous fluctuations of two velocity components were recorded for all vertical locations at a single fetch. The water surface drift velocity was determined by the particle tracking velocimetry (PTV) method. Evaluation of spatial growth rates of waves at various frequencies was performed using wave gauge records at various fetches. Phase relations between various signals were established by cross-spectral analysis. Waves' celerities and pressure fluctuation phase lags relative to the surface elevation were determined. Pressure values at the water surface were determined by extrapolating the measured vertical profile of pressure fluctuations to the mean water level and used to calculate the form drag and consequently the energy transfer rates from wind to waves. Directly obtained spatial growth rates were compared with those obtained from energy transfer calculations, as well as with previously available data.

**Key words:** air/sea interactions, turbulent boundary layers, wind–wave interactions

---

## 1. Introduction

The problem of water waves' generation by wind is the focus of this work. Over the past few decades, the increasing demand for marine transportation safety together with the emerging desire to harvest the ecologically clean waves' energy has motivated extensive research of the problem during the last century. An accurate quantitative description of the problem of waves' generation by wind has become necessary in order to clarify mechanisms governing the energy transfer from wind to waves. Understanding the ocean–atmosphere momentum exchange is also of high importance in view of the accuracy of both synoptic and mesoscale weather prediction models.

<sup>†</sup> Present address: University of Notre Dame, Civil Engineering and Geological Sciences, University of Notre Dame, Notre Dame, IN 46556, USA. Email address for correspondence: dan.liberzon.1@nd.edu

In the simplest case of wind-exited deep-water waves, propagating without significant energy loss over long distances under steady blowing turbulent wind, both spatial and temporal evolution characteristics of the wave field are directly governed by the wind energy input and the nonlinear wave-wave interactions (Young 1999; Janssen 2004). In turn, the boundary conditions at the water surface that affect the airflow vary due to wave field evolution and surface currents induced in water by the shear flow in the air. The problem of decoupling the background turbulent fluctuations in the airflow and those induced by the water surface movement thus becomes quite complicated. The mean wind flow is assumed to be horizontal and contains both turbulent and wave-induced fluctuations of air velocity and pressure. It is generally assumed that the structure of the mean flow above an air-water interface can be described as similar to that of the turbulent flow above a stationary/moving rough surface (see e.g. Shlichting & Gersten 2000), although apparently important differences between these two flows exist, mainly due to unsteadiness of the interface and essential difference in the boundary conditions. Above a thin viscous sublayer, the mean wind velocity  $U(z)$  changes logarithmically with the height above the mean water level.

The turbulent nature of the wind, and limited abilities to perform accurate measurements in close proximity to the constantly varying water surface, pose a serious challenge in evaluating the wave-induced variations in the air velocity vector. To express the extent of the accumulated wind effect on the wave field, a notion 'wave age' is often used, defined as the ratio between the celerity of dominant waves and the wind friction velocity,  $c/u_*$  (see e.g. Plant 1982; Janssen 2004). At the initial stages of wave generation, when the water surface is characterized by shorter waves with low celerities, the wave age values are below unity. The wave age increases as the wind continues to blow and the dominant waves get longer; values exceeding unity characterize transition sea conditions: a mature sea is characterized by wave age exceeding 10.

The history of scientific publications on generation of waves by wind starts almost a century ago (Jeffreys 1925). Major progress was made in 1957 when two groundbreaking works of Miles and Phillips appeared. Published simultaneously but independently, these studies presented two different models describing governing mechanisms of water-wave generation by wind: the resonant model by Phillips (1957) and the shear flow model by Miles (1957). The resonant model introduced by Phillips (1957) attributed the waves' excitation and growth to air pressure fluctuations governed by the convection of turbulent eddies. The water is assumed to be inviscid and at rest at the time of wind inception. The initially calm water is disturbed by the turbulent wind, the component of the surface pressure distribution that moves at the speed of a free surface wave with the same wavenumber will create the initial roughness; the resulting waves, being in resonance with the pressure fluctuations, grow in time. The pressure field is convected across the water surface and slowly evolves due to interactions between eddies. The resonant model predicts linear growth of waves' energy. It was also advocated that as the waves' amplitude grows, the sheltering effect suggested by Jeffreys (1925) starts to play an increasingly important role and should be also accounted for. At longer times, the sheltering from the wind at the lee side of waves of sufficient height causes the resonance mechanism to become insignificant. Experimental validation of the resonant model requires juxtaposing wave and spatial pressure fluctuation spectra, a goal that is extremely difficult to achieve. Also, the validity of the model is limited because it disregards the coupling between air and water flows.

The shear flow model was introduced by Miles (1957), with further developments introduced later (Miles 1959, 1965, 1993). Assuming that water is an inviscid fluid initially at rest, the wave growth was attributed to waves' interaction with the parallel air shear flow. Miles demonstrated that the rate of energy transfer to a wave component propagating at phase velocity  $c$  is proportional to the wind profile curvature  $U''(z_{cr})$  at the critical height where the wind speed equals the phase velocity of the wave,  $U(z_{cr}) = c$ . While temporal growth rate of waves is linear according to Phillip's resonant model, Miles' shear flow model predicts exponential growth. In Miles (1959), several improvements to the shear flow model were introduced, such as applying the airflow boundary conditions on the curved water surface. Application of a more accurate numerical model resulted in a smaller temporal growth rate as compared to that in Miles (1957). Later, the accuracy of numerical solutions was improved further by Conte & Miles (1959). The theoretical effort originated by Miles was continued by numerous publications during the last few decades. Janssen (1989) presented a quasi-linear theory of wind-wave generation, together with numerical calculations for a steady state case. The similarity to the flow above stationary hills was utilized by Belcher & Wood (1996) for development of a theoretical model for drag calculations in the airflow above two-dimensional waves. Belcher & Hunt (1998) reviewed the mechanisms controlling turbulent boundary-layer flow over hills and waves and compared calculations based on various analytical models and available experimental data. They stressed the importance of the airflow separation for drag estimations. Mastenbroek *et al.* (1996) also considered the second-order effects; their inclusion in the analysis resulted in improved momentum flux estimations in comparison with experimental data available at that time. Reutov & Troitskaya (1996) presented a quasi-linear theoretical model using a gradient first-order approximation for turbulent stresses and isotropic viscosity. Waves' temporal growth rates predicted in their model were somewhat higher than those of Miles (1957, 1959). The decrease in waves' growth rate with wind speed and wave steepness in mature sea was attributed by Kudryavtsev, Makin & Meirink (2001) to an increased role of nonlinear interactions under those conditions. Athanassiadou (2003) suggested an improvement to the linear model introducing the term representing the effect of turbulence on the drag. The dependence of drag on wave regime (age and steepness) was shown and numerical results for a simple sinusoidal wave were presented. Theoretical work of Stiassnie, Agnon & Janssen (2007) circumvents the apparent critical-layer singularity through Rayleigh's instability equation solution. Computed spatial growth rates were in good agreement with previously available results from experimental data and with Miles' (1957) predictions.

Evolution of short gravity-capillary waves at the initial stages of water waves' generation by wind has attracted particular interest since the late 1950s. Benjamin (1959) presented a solution of the Orr-Sommerfeld equation emphasizing the importance of the air viscosity role in mechanisms governing the shorter waves growth. By numerically solving a coupled viscous model, while disregarding the Reynolds stresses, Valenzuela (1976) found a reasonable agreement between his results and the shear-flow model. Including the water current in his model resulted in higher growth rates for waves with smaller wavenumbers and for higher wind speeds, as compared to the Miles' predictions. Later works (Kawai 1979; van Gastel, Janssen & Komen 1985; Janssen 1986) emphasized the role of the water shear current that modifies the gravity-capillary dispersion relation due to the Doppler shift effect, caused by the current. The importance of the induced current was further emphasized by Caulliez, Ricci & Dupont (1998). They experimentally

studied the first visible wind waves and observed an 'explosive' growth related to the three-dimensional instability and the laminar–turbulent transition in the drift current.

During the last few decades, a substantial effort was made to accumulate large amount of reliable and accurate experimental data in order to validate models for wave generation by wind. Despite advances in measurement techniques and instrumentation, conducting accurate and reliable measurements both in the airflow and the water remains a very demanding task. To evaluate the actual growth rates of water waves and the energy transfer rates from wind to waves, various parameters of water and airflows should be accurately measured. The instantaneous water surface elevation, water surface velocity and the velocity profile in water are among the most important parameters characterizing the 'water side' of the problem. To get a complete description of the airflow above water waves, it is essential, besides accumulating accurate data on the variation of mean wind speed with height and on the wind direction, to carry out reliable measurements of the pressure fluctuations as well as of air velocity components in the turbulent wind flow. In order to estimate temporal growth rates of waves under various wind-forcing conditions, all necessary parameters should be measured simultaneously and at sufficiently high sampling rates. In addition, characteristic times of wind-wave field variation are usually quite short as compared to the response time of the experimental facility to the variation of the wind-generating parameters. Therefore, the direct monitoring of waves' temporal evolution is especially difficult. This is particularly so for the initial stages of waves excitation for which the characteristic times are shorter. Estimation of the spatial evolution under steadily blowing wind requires measurements at various locations along the water-wave field.

Field experiments by Snyder (1974) and Snyder *et al.* (1981) produced results showing wave growth rates higher than those predicted by Miles' model, but of the same order of magnitude. The difference was higher for relatively low-frequency waves for which the phase velocities of dominant waves are close to the forcing wind speed measured at the representative height of  $z=10$  m,  $U_{10}$ . Larson & Wright (1974) performed laboratory measurements of the initial temporal growth rates following impulsively applied wind forcing for waves with fixed lengths ranging from 7.2 to 70 mm. Both temporal and spatial evolution of waves was investigated by Plant & Wright (1977) using Doppler radar spectrometry; waves propagating in along- and counter-wind directions were examined. Both growth rates appeared to be exponential and equal for short gravity–capillary waves of small amplitudes. Plant (1982) summarized the available up-to-date results accumulated in numerous field and laboratory experiments. Presenting the non-dimensional temporal growth rates of wave energy as a function of the reversed wave age  $u_*/c$  set the style for data comparison that was widely used in later works. Hsu & Hsu (1983) and Papadimitrakakis, Hsu & Street (1986) collected experimental data on the structure of the wave-induced velocity and pressure fields in the airflow over mechanically generated waves. Investigation of the wave-induced vertical profile of the air velocity and pressure was performed by Hare *et al.* (1997). Results of an experiment in the open sea were compared with previously available data and theoretical analysis, including detailed examination of the wave-induced air velocity vertical component and pressure fluctuations. Decay of wave-induced velocity fluctuations with height, as well as the phase relations with water surface elevation, was discussed. Uz *et al.* (2003) performed laboratory experiments evaluating growth rates of gravity–capillary waves under transient wind forcing. All wave components were reported to grow

exponentially, and growth rate variation with wind speed and stress fluctuations was examined. Measurements performed by Hristov, Miller & Friehe (2003) at an open sea-positioned platform supplied evidence for existence of the critical-layer mechanism for mature seas ( $16 < c/u_* < 40$ ). Analysing the available field measurement data, Agnon *et al.* (2005) found that the skewness and the asymmetry of wind waves vary on the fine temporal and spatial scales, suggesting the necessity of new approaches for the interpretation of measured data. Wind-generated wave growth at short fetches was investigated by Lamont-Smith & Waseda (2008) using experimental data collected in large wave tank. Comparing the results with those available from field measurements, only limited agreement was revealed regarding the growth rate dependence on fetch. Caulliez, Makin & Kudryavtsev (2008) investigated numerous wind–waves coupling parameters performing measurements of the wind waves excited in the laboratory at relatively short fetches and comparing the results with available models. They suggested correcting the mean wind velocity values in view of the mean water surface current which was assumed in this study to constitute 2.5 % of  $U_{10}$ . The water surface roughness was shown to vary with both the wind speed and the fetch. Young waves were shown to be characterized by relatively high steepness of dominant wave components, as compared to available measurement results in mature sea conditions.

Reul, Branger & Giovanangeli (1999, 2008) investigated the role of the breakers in the airflow separation process using the particle image velocimetry (PIV) technique. It was shown that tangential stress decreases on the lee side of the wave due to the separation and then grows towards the next wave crest. Veron, Saxena & Misra (2007) performed PIV measurements of the airflow in the wind–wave tank to document the airflow separation above short wind-generated waves. As a result of the flow separation, a significant viscous stress reduction was observed in the separated region, leading to the substantial variation of the stress along the wave. Peirson & Garcia (2008) investigated mechanically generated steep and breaking waves, observing reduction in the growth rate with waves' steepness. By carrying out a detailed comparison with previous works, they demonstrated the significance of waves' mean steepness in determining the wind to wave energy transfer rates. Shaikh & Siddiqui (2008) and Troitskaya *et al.* (2010) used the PIV technique to investigate the airflow in close proximity to the waves' surface. Shaikh & Siddiqui (2008) found a significant increase in the vorticity and the energy dissipation at elevations bounded by waves' crests and troughs, accompanied by a maximum in turbulent energy production at vertical distances from the interface of the order of significant wave heights. Troitskaya *et al.* (2010) reported good agreement of experimental results with the model of Reutov & Troitskaya (1996). No separation of the airflow was detected for the experimental conditions examined in this study.

Accurate quantitative measurements of the pressure fluctuations in time at different locations within the wave field are extremely important for understanding the wind–wave interactions (Phillips 1957; Janssen 2004). However, measurements of the static pressure fluctuations within the turbulent airflow boundary layer above water waves are quite complicated, as they require decoupling of the static pressure fluctuations from the (generally significantly stronger) fluctuations of the dynamic pressure within the boundary layer. Accurate and reliable measurements of the static pressure fluctuations thus require a probe that is insensitive to the mean and fluctuating dynamic pressure and to variations in the mean flow direction. Over the past few decades, a number of static pressure measurement techniques, all using in-house

made devices, were suggested. One of the most popular designs used is the 'disk-type' probe (Robertson 1972; Gill 1976; Nishiyama & Bedard 1991; Mastenbroek *et al.* 1996; Hare *et al.* 1997; Wilczak & Bedard 2004). At higher wind velocities, the disk-type pressure probes require larger disk diameter for efficient dynamic pressure elimination, thus making such a design less suitable for use in laboratory-scale wind-wave flumes. A different version of the disk probe, designed for laboratory use, was proposed by Elliot (1972). The Elliot probe features streamlined upper and lower surfaces, introducing improved dynamic pressure elimination, while preserving small probe diameter. The Elliot probe was used successfully in numerous studies by Donelan *et al.* (1999, 2005, 2006). An up-to-date review of the available static pressure instrumentation can be found in Liberzon & Shemer (2010), which suggested using a commercially available sensor for wind-wave studies.

As the energy is being transferred from wind to water waves, a surface current is also created due to the shear stress induced by the wind blowing over the water surface, as well as due to waves' nonlinearity. Hence, the water velocity profile is developed beneath the surface and propagating waves are affected by the water motion. The depth of this influence depends on waves' characteristics such as length and amplitude. Studying the processes related to waves' excitation and growth under wind action thus requires accurate estimation of the water velocity profile as a function of depth. Of particular importance is the water surface velocity as it provides the boundary condition for the forcing wind. In addition, air and water temperatures should be evaluated, and the occurrence of waves' breaking and resulting surface discontinuities should be accounted for. Since the use of intrusive methods for measuring surface velocity of water may disturb the velocity field both in water and air, a variety of non-intrusive measurement techniques were developed and implemented over recent years. These techniques include particle and tracers tracking and thermal imaging. An early laboratory study of Wu (1975) implementing dye tracing suggested a linear profile of water velocity. Therefore, surface velocities were estimated by extrapolation of the measured values below the surface. PIV allows accurate mapping of water velocity field but presents substantial difficulties when approaching the water-air interface due to limitations on particle size and the presence of optical distortions in that region. Banner & Peirson (1998) performed PIV measurements of the wind-driven wave field in the presence of waves' breaking. Making use of two synchronized PIV cameras for simultaneous water surface imaging they have produced a large set of data, mapping the water velocity and shear within 200  $\mu\text{m}$  from the water surface. Using combination of PIV and particle tracking velocimetry (PTV) techniques, Herring *et al.* (1998) investigated water velocity components and turbulence levels at depths of up to 1 mm beneath the wavy water surface. Infra-red (IR) imaging devices are also being used for water surface velocity measurements by means of monitoring the propagation of heated spots on the water surface. Such a technique is favourable in controlled laboratory conditions, when the water surface and air temperatures remain constant. Jessup & Zappa (1997) also used IR camera monitoring of thermal signature for conducting an experimental investigation of a 10  $\mu\text{m}$  thin water surface sublayer under breaking waves. Siddiqui *et al.* (2001) produced simultaneous measurements of water surface velocity components using an IR camera and in water velocity profiles using PIV. By illuminating the water surface with a laser, the thermal nature of micro breaks on wind-generated waves was investigated and correlated with the appearance of vortices formed behind the leading edge of the breaker. Siddiqui & Loewen (2007, 2009) used PIV and IR techniques simultaneously to investigate the water drift layer below surface wind-generated waves, particularly at the events of

waves' microscale breaking. Averaging measured data over waves' phases allowed derivation of the spatial distribution of water turbulence parameters along the wave. Veron & Mellville (2001) and Veron, Melville & Lenain (2008, 2009) investigated the stability of the wind-driven water surface, the effects of Langmuir instabilities and of temperature variations on turbulence generation. An IR camera was used in laboratory and field experiments to monitor the water surface temperature and to map the surface velocities through monitoring thermal signature from laser-generated hot spots.

Conducting field experiments in the open sea is, generally speaking, preferable as the collected data provide information on the measured parameters at natural scales. The unstable nature of the wind, and especially the limited ability to predict weather conditions, are only two of the major obstacles encountered in field measurements. The necessity to mount the equipment on a stable platform further complicates the experiment and leads to considerable operational costs. Hence, such experiments are often conducted at relatively small lakes (Donelan *et al.* 2005, 2006) or at the near-shore locations (Snyder *et al.* 1981). The operational restrictions on field measurements often lead to limited fetches and water depths. To carry out field experiments at somewhat reduced costs, the use of floating (instead of fixed) platforms is being practiced (Donelan *et al.* 1999; Hristov *et al.* 2003). Operating experimental set-ups mounted on floating platforms, however, poses numerous technical challenges. Elimination of the unwanted contamination of the recorded signals as a result of the platform movement with the water surface and accurate vertical positioning of the instruments in such set-ups are rather difficult and require implementation of sophisticated techniques. The unknown waiting times for preferable weather conditions, limited repeatability and reduced data accuracy characterize the open sea experiments.

An alternative to the field experiments is conducting the experiments in specially constructed wind-wave flumes. Laboratory experimental facilities offer the advantages of controlled environment at a reasonable cost, as well as numerous additional advantages. Among the most prominent is the possibility to create stable and steady airflow at a wide range of air velocities. Positioning the sensors at accurate vertical locations is possible both in respect to the mean water surface and to the instantaneous surface elevation using wave followers (Shemdin & Hsu 1967; Papadimitrakakis *et al.* 1986; Mastenbroek *et al.* 1996; Donelan *et al.* 1999, 2005, 2006). To attain reasonably high airflow velocities matching the open sea values, relatively large blowers may be needed. However, since the wave generation by wind is primarily governed by the airflow parameters in the close vicinity of the air-water interface, this restriction can be eliminated by reducing the cross-sectional area of the airflow, while keeping the airflow section height significantly larger than the waves' amplitudes.

Despite more than half a century of experimental research of water waves by wind excitation and evolution, substantial gaps in understanding the physical mechanisms that govern these phenomena still exist. Both the resonant model of Phillips, applicable probably only for shorter waves, and the Miles' shear flow model were shown to be limited in predicting the waves' growth rates. Substantial theoretical effort is required to arrive at better understanding of the problem. Filling the substantial gap in experimental data was the primary goal of the present work. We report on a laboratory study aimed at accumulation of extensive quantitative and qualitative data of parameters that govern water waves' generation by wind. In view of the limited size of the laboratory flume, the initial stages of the process are investigated.

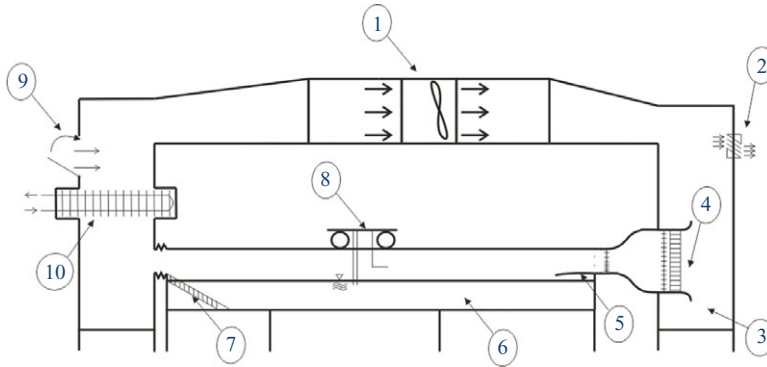


FIGURE 1. (Colour online available at [journals.cambridge.org/FLM](http://journals.cambridge.org/FLM)) Wind-wave flume scheme: (1) blower; (2) flow rate control hatch; (3) settling chamber; (4) contraction with honeycomb and nets; (5) flap; (6) test section; (7) beach; (8) instruments carriage; (9) maintenance hatch; (10) heat exchanger.

## 2. Experimental set-up

The experiments were performed in a small-scale wind-wave flume that allows generation of strong turbulent wind at velocities comparable with those measured in open sea under quite extreme conditions. The experimental facility is sufficiently long for the study of initial stages of spatial water-wave evolution and enables easy access to the test section for instrumentation installation. The facility has a two-level configuration, with the wind tunnel mounted atop the wave tank, see figure 1. The closed loop airflow and the heat exchanger allowed achieving constant temperature and humidity of the airflow in the course of experimental runs. To eliminate translation of any mechanical vibrations that may originate in the blower to the test section, all main parts of the facility, i.e. the test section, the blower, and both the inlet and the outlet air guiding channels, were separated by flexible vibration-dumping connections.

The test section is enclosed within a frame made of aluminium extrusions and is supported by eight legs, each equipped with shock-absorbing pads. The 5 m long, 0.4 m wide and 0.5 m deep test section is made of clear reinforced 6 mm thick glass plates. Clear glass walls of the tank mounted on the frame allow viewing of the flow from any desired angle. Rectangular air inlet and outlet openings in the tank are 0.4 m wide and 0.25 m high, thus limiting the maximum water depth to 0.25 m. A wave energy absorbing beach made of porous packing material is located at the far end of the tank and effectively prevents wave reflection. Openings in the tank floor at each end of the test section allow tank filling and draining via a 1  $\mu$ m particle filter and a UV water sterilizer. The water surface was skimmed prior to each experimental run, to ensure removal of surface film that can affect results in view of the relatively short waves characteristic of this study.

The test section roof is made of a number of removable 1 m long Perspex plates with a 3 cm wide slot in the centre sealed by fine brushes. Use of clear Perspex allowed visualization of the water surface from above, while the slot is used to introduce sensors into the test section at any distance from the inlet. The brushes in the roof slot allow easy movement of the instrument carriage that can be fixed at any desired fetch.



A centrifugal, 7.5 HP, blower allows attaining mean airflow velocities in the test section of up to  $13 \text{ m s}^{-1}$ . The blower is capable of supplying airflow rate of 4200 c.f.m. and is controlled by a frequency modulator through either a manual pad or a PC-generated signal. Silencer boxes with a volume of about  $1 \text{ m}^3$ , padded with sound-absorbing material, installed at both sides of the blower proved to be very effective in reducing the noise and smoothing the flow at the blower exit.

Care was taken to ensure uniform air velocity distribution at the inlet to the test section. A large settling chamber with the volume of about  $1 \text{ m}^3$  is located at the inlet of the test section (figure 1, element 3). A similar settling chamber is also installed at the test section outlet. In the inlet settling chamber, the airflow comes virtually to rest and is guided through a 5 cm thick honeycomb with 5 mm hexagon cells into a nozzle with the area reduction ratio of about 4, yielding an essentially parallel and uniform flow at the entrance of the test section. To eliminate water flow into the settling chamber, the lower edge of the nozzle is located 7 cm above the designed water level. A 40 cm long flap provides smooth expansion of the airflow cross-section between the nozzle and the mean water surface elevation. The large outlet settling chamber effectively eliminates fluctuations of back pressure; it is equipped with a drainage system, allowing removal of any water that may accumulate during the experiments as a result of spraying or water vapour condensation. The maintenance hatch installed in the back of the outlet settling chamber allows access to the blower. A heat exchanger installed in the outlet settling chamber operates using cold ( $\sim 8^\circ\text{C}$ ) water supply from the main and a PC-connected controller. The heat exchanger allows maintaining the air temperature constant within  $\pm 2^\circ\text{C}$ .

The instruments carriage that is build of aluminium extrusions and is installed on a rail, mounted along the test section, supports the measuring equipment, the power supplies and the sensors. The carriage position along the test section at the desired fetch is the only experimental parameter controlled manually. The wave gauges and the airflow sensors are mounted on two separate vertical traverse systems. Both traverse systems driven by a pair of identical PC-controlled step motors have a positioning accuracy of  $50 \text{ }\mu\text{m}$ . The shorter traverse with the total stroke of 70 mm was used for positioning the wave gauges, while the longer one (450 mm stroke) was used for positioning the airflow sensors (Pitot tube, static pressure probe and hot-film sensor). All airflow sensors were located on a horizontally levelled rack around the centreline of the test section with the horizontal spacing of about 2 cm between the adjacent probes. An additional maximum wave height sensor was used to attain accurate positioning of the airflow-sensing instruments relative to the constantly varying water-wave surface and to eliminate undesirable wetting of the air-measuring instruments. The sensor consists of two parallel copper wires with exposed tips placed 5 mm below the air sensors and connected to a 1.5 V voltage source through a  $20 \text{ k}\Omega$  resistor. As long as the wires' tips remain dry, the electrical circuit is open; wetting of the tips closes the electrical circuit and causes a detectible voltage drop on the resistor. The lowest position of the airflow sensors above the water surface is limited by the sensors' size to 5 mm. To allow accurate positioning of the sensors at the desired vertical position above the waves, the instantaneous surface elevation of the highest wave was determined for each set of experimental conditions. To this end, computer-controlled incremental search of the highest wave was performed starting from a safe position above the wave field. At each step, the rack was moved down by a prescribed increment and the output voltage was sampled for the prescribed duration of time (3 min). If no voltage drop was detected on the maximum wave height sensor during the recording session, indicating that the sensor tip remained

dry throughout the whole sampling duration, the rack was moved to the next lower position. Once the tips of the wires became wet, the rack was moved up by a halved increment and a new series of incremental movements down with the reduced step were performed. The procedure was repeated until the elevation of the local highest possible wave was detected with the accuracy of 0.1 mm. Once the actual highest wave height above the mean water level was found at a later stage from the wave gauge records, the exact vertical location of sensors above the mean water surface level was established.

Analogue signals from all instruments used during the experiments were digitized by a pair of A/D cards and recorded by a PC. Water and air temperatures and relative air humidity were monitored using commercially available sensors.

Instantaneous water surface elevation variations were measured by capacitance-type wave gauges. Following Chapmann & Monaldo (1995), anodized tantalum wire 0.5 mm in diameter was used. A five channels custom-made conditional unit converted wave gauge capacitance variations due to the change in the instantaneous water level into output voltage fluctuations in the range of  $\pm 10$  V. The vertical traverse was used to calibrate the gauges statically at prescribed submerged depths in still water. Two consecutive wave gauges mounted on a rigid holder spaced by 14 mm along the tank were used.

Two pressure-sensing instruments were used during the experiments, a static pressure probe and a Pitot tube. Two identical differential pressure transducers (PR274, MAMAC Systems Inc.) were used for both sensors. The transducer is capable of sensing small pressure variation (less than  $2.5 \times 10^{-5}$  Pa) in three adjustable ranges (32, 64 and 125 Pa). The output voltage of the transducer varies linearly with the sensed pressure in the range of  $\pm 5$  V. Digitizing the transducer signal by a 12 bit A/D ( $\pm 10$  V range) card yields pressure measurement accuracy of 0.01, 0.02 and 0.04 Pa, respectively, for each range.

A single-ended, 1 mm ID and 1.5 mm ED, home-made Pitot tube was used to measure mean air velocity. The tube is curved by  $90^\circ$  to be introduced to the airflow from above, and the back end of the tube is connected via a wider (3 mm ID) 30 cm long flexible Tygon tube to the high pressure sensing port of the pressure transducer. The low-pressure port is connected by a similar flexible tube to a box placed within the test section close to the roof at the same fetch and filled with sponge. The dynamic pressure  $\Delta P$  that is the difference between the Pitot-tube sensed total pressure and the static pressure at the same fetch is translated by the transducer into an analogue voltage signal. At initial stages the transducer output was validated against an accurate alcohol manometer. The Pitot tube measured mean velocities were also used for the hot-wire sensor calibration.

To produce accurate static pressure variation measurements close to the water surface, a commercially available static pressure probe (A520, MAMAC Systems Inc) was used. For a full description of the static pressure probe characteristics and validation tests performed, see Liberzon & Shemer (2010) and Liberzon (2010).

To measure variations in both the vertical and the horizontal airflow velocity components, an X-hot film (HF) probe (TSI T-1241-20) together with a commercially available multichannel anemometer (AA Lab Systems) was used. Since the HF measurements were performed in a strongly sheared flow, with mean velocity at any given fetch and airflow rate in the test section changing with the vertical position and ranging from close to zero to the maximum velocity in the central part of the wind tunnel, the hot film was calibrated for the correspondingly wide range of air velocities. *In situ* calibration was performed with the sensor placed in the central part

of the wind tunnel against the Pitot tube placed at identical elevation. The mean air velocity was varied within the desired range by controlling the blower.

Prior to actual measurements, parameters characterizing the experimental system (e.g. wind velocity stabilization times, pressure drop along the flume and uniformity of wave field parameters across the tank) were determined. Series of tests were performed to validate sensing instruments functioning in view of the expected experimental conditions (Liberzon 2010; Liberzon & Shemer 2010). A full description of the experimental facility is given in Liberzon (2010).

### 3. Experimental procedures and conditions

Simultaneous measurements of multiple parameters of both the airflow and the water waves were performed. Mounting all sensors on the instrument carriage allowed measurements to be performed at any selected fetch along the wave tank for a wide range of wind flow rates. Automated calibration of sensors and vertical positioning of the air-sensing instruments by means of PC-controlled motorized traversing mechanisms allowed scanning of airflow parameters at multiple heights above the waves. To ensure repeatability and consistency of data acquired at various fetches, a standardized procedure was established. A special effort was made to ensure accurate determination of the vertical position of the air-sensing instruments above the mean water surface that is dependent on the experimental conditions. The instruments carriage was positioned manually at the desired fetch and a full set of measurements was then performed for the prescribed wind speeds. Measurements were carried out at nine fetches along the tank:  $x = 100, 140, 160, 180, 220, 260, 300, 340$  and  $380$  cm. The complete set of data was collected for four prescribed airflow rates corresponding to the blower controller frequencies of 25, 35, 45 and 55 Hz. Vertical profiles and various airflow parameters were obtained by the Pitot tube, the static pressure probe and, on some occasions, also by the hot film anemometer at 38 vertical positions above the wavy water surface, ranging from 5 mm above the highest possible wave at the current experimental conditions, up to the highest measuring location at 190 mm above the highest wave. During each of the 38 measurements of the airflow parameters at a given fetch and airflow rate, the instantaneous water surface elevation variations were recorded simultaneously by the two consecutive wave gauges. All individual records were 180 s duration; the sampling frequency used was 120 Hz unless stated otherwise. The data acquisition procedure at a fixed fetch consisted of the following steps.

- (i) Wave gauge calibration in view of the expected wave height ranges for the given wind flow rates.
- (ii) Running the blower at a prescribed airflow rate for a sufficient time (40 min) to attain constant air and water temperature.
- (iii) When relevant, *in situ* calibration of the X-hot-film thermoanemometer for the expected range of air velocities.
- (iv) Resetting the blower to operate at the prescribed flow rate for at least 3 min to reach a quasi-steady wave field state.
- (v) Positioning the airflow sensing instruments rack at the safe elevation above the waves, followed by accurate determination of the rack's height above the highest wave in the generated wave field. Repositioning the rack at the desired vertical position.
- (vi) Performing a set of simultaneous measurements of the instantaneous water surface elevation by wave gauges, mean wind speed by the Pitot tube, instantaneous static pressure fluctuations by the static pressure probe, air and water temperature,

air humidity, and on some occasions two air velocity component fluctuations by the X-film thermoanemometer. The records of all sensors were stored on the PC hard drive for later processing.

(vii) Moving the air-sensing instruments to the next vertical position and repeating the measurements until a complete record of the vertical profile of all airflow parameters had been accumulated.

(viii) Repeating steps (i–vii) for all prescribed wind velocities.

Each set of measurements conducted at the given fetch lasted for about 16 h (for four different wind velocities) and was performed utilizing LabView<sup>®</sup> software without human intervention. To prevent accidental storage of faulty data, a number of essential parameters that may indicate failure in the experimental procedure were continuously monitored by the software. For example, pressure readings from the Pitot tube or the static pressure probe beyond the expected range may indicate that the instruments became wet; air temperature control during HF calibration may indicate blower overheat or temperature sensors failure; thermoanemometer readings out of the calibration range may indicate electronics failure or an extreme change in room temperature, etc.

The vertical coordinates  $z$  of the probes relative to the mean water level for each measurement were obtained by adding the measured corresponding maximum crest height to the vertical coordinate above the crest known from sensors positioning procedure described above. The mean wind velocity at each vertical position above the waves was determined by averaging the Pitot tube-derived velocity records. For all four flow rates examined, the mean airflow velocity increased with the distance from the water–air interface up to the maximum value  $U_{max}$  and then decreased due to the presence of the roof. Since the roof is not hermetically sealed, a small drop in the flow rate, resulting in less than 10 % drop in  $U_{max}$  values along the test section, was detected. The averaged along the tank maximum velocities, used as the corresponding representative values, were  $U_{max} = 4.54, 6.38, 8.21$  and  $10.05$  ( $\text{m s}^{-1}$ ), respectively. Values of  $U_{max}$  at each fetch increased linearly with the blower controller frequency.

To determine the boundary condition at the mean water elevation, the water surface velocity was measured separately by PTV. Small tracers were seeded on the water surface and imaged by a video camera mounted on the instrument carriage. To function as a reliable water surface velocity tracer, the particle must be light-weighted to prevent sinking during the propagation along the flume, flat to minimize the wind-induced stresses influence on particle velocity and made of non-toxic/contaminating inexpensive material. After several trials, small round paper disks produced in large quantities using a simple paper puncher were chosen to function as the surface velocity tracers. The paper disks were observed to be sufficiently flat and buoyant to remain on the water surface during their propagation through the view field of the camera. Water velocity was measured at several fetches up to  $x = 410$  cm from the entrance to the test section. For each measurement about 350–400 tracers cut from black paper were used. The tracers were dispensed a few millimetres above the water surface through a long dry pipe introduced into the test section through the slot along the middle of the test section; the particles settled on the water surface 15–20 cm upstream of the imaged area. Two 500 W halogen lamps illuminated the imaged area; white paper sheets were used to cover the sidewalls and the bottom of the tank in the imaged area to scatter the light and to attain a more uniform illumination. The illumination and the exposure parameters were adjusted to get clear and bright pictures of the water surface, while the image of the black tracers contrasted strongly

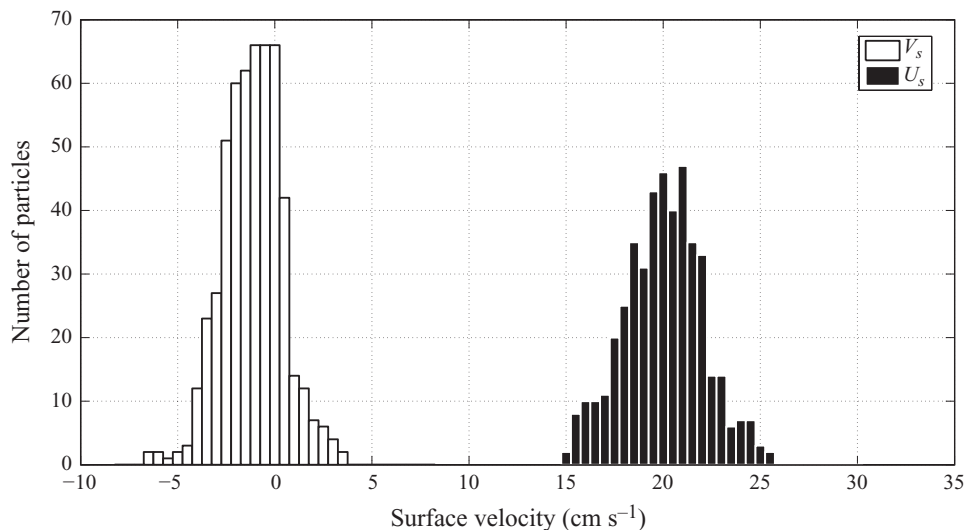


FIGURE 2. Histograms of the PTV-derived along wind,  $U_s$  and across-wind,  $V_s$  surface velocity components. Fetch  $x = 50$  cm and  $U_{max} = 6.38$  m s<sup>-1</sup>.

with the background. The resolution of the camera was  $640 \times 480$  pixels for the 15 cm long imaged area and the recording was performed at 60 f.p.s. The recorded video clips allowed monitoring each particle's trajectory and calculating particle's velocity components along and across the imaged section. Although the majority of the seeded particles remained on the water surface during their propagation across the camera field of view, a relatively small portion of particles was immediately submerged due to rapid wetting and/or wave breaking. Submerged particles either settle on the bottom of the tank causing zero velocity detection by the PTV or move at notably slower than surface velocities. To eliminate the contribution of the submerged particles to the measured drift velocity, advantage was taken of the fact that such particles are out of focus and are seen as blurred spots in the images. An image processing routine was developed that removes such particles from the ensemble. Particles' positions were collected from each frame and consequently two velocity components,  $U_s$  and  $V_s$ , were tracked across all frames of appearance using the particle tracing Matlab<sup>®</sup> toolbox. Mean values were calculated from each velocity distribution. A representative distribution of particles' velocities is presented in figure 2.

## 4. Results

### 4.1. Characterization of the airflow

To enable comparison of the present experimental results with earlier measurements carried out in open sea and laboratory, as well as with theoretical predictions, both the airflow and the wind-wave field should be parameterized appropriately. To obtain a common reference for the vertical profiles of airflow parameters, the mean surface elevation for all waves recorded at any given fetch and airflow rate with the total duration of 38 times 180 s, i.e. 6840 s, or nearly 2 h, was calculated and the highest measured crest height determined. The maximum measured crest heights increased with the flow rate and the fetch. The mean water surface drift velocity  $U_s$  constitutes the boundary condition at  $z = 0$  for the vertical air velocity profile. While the PTV-derived mean values of the cross-wind surface velocity  $V_s$  are close to zero as expected

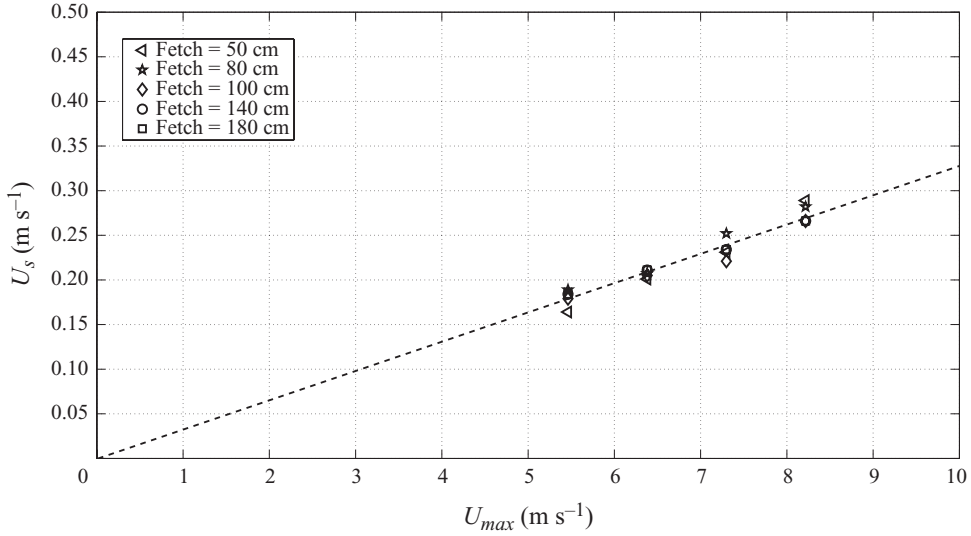


FIGURE 3. Water surface velocity  $U_s$ . Dashed line, linear fit;  $U_s = 0.033U_{max}$ .

(figure 2), the along-wind component of the surface velocity  $U_s$  is quite significant. The variation along the tank of  $U_s$  is plotted in figure 3 as a function of  $U_{max}$ . The measured surface drift velocities are in general agreement with the results of Peirson (1997) obtained using PIV at comparable experimental conditions.

The values of  $U_s$  vary linearly with wind speed, and deviations from the linear fit in the measured mean values of  $U_s$  at each fetch are of the order of few centimetres per second, within the expected PTV accuracy. The Pitot tube measured mean airflow velocities always exceed  $1 \text{ m s}^{-1}$ , even at the lowest measuring location; therefore, this error in the PTV measured mean values of  $U_s$  as representing the boundary condition at the water–air interface is negligible. At longer fetches, beyond about 200 cm, and under stronger winds, relatively high waves' amplitudes and an increasing number of breaking events prevented performing reliable measurements using the adopted visualization technique. The mean surface velocity values  $U_s$  corresponding to the higher wind flow rates and farther away from the test section inlet were therefore estimated from the linear fit in figure 3.

The surface drift velocity constitutes slightly above 3 % of the maximum air velocity in the cross-section. To account for the non-zero mean velocity at the air–water interface, an airflow velocity  $U_a$  was taken relative to the water surface velocity  $U_s$ ,

$$U_a = U_{absolute} - U_s, \quad (4.1)$$

similar to Caulliez *et al.* (2008). For the turbulent airflow in the test section, the mean wind velocity is expected to exhibit a logarithmic profile

$$U(z) = \frac{u_*}{\kappa} \ln \left( \frac{z}{z_0} \right) \quad (4.2)$$

for a specific range of heights above the mean water surface.

This profile is characterized by two parameters: the friction velocity  $u_*$  and the water surface roughness  $z_0$ ,  $\kappa = 0.41$  being the von Kármán constant. The measured profiles of  $U_a$  exhibit logarithmic behaviour close to the water surface, usually up

Fetch (cm)	100	140	160	180	220	260	300	340	380	Mean
$f_{bl}$ (Hz)										
25	7.87	8.44	8.46	8.78	9.02	9.13	9.37	9.51	10.13	8.60
35	13.48	13.66	12.83	13.65	13.48	13.65	13.43	14.13	14.13	13.03
45	18.48	18.50	17.88	19.38	17.48	17.32	16.94	17.61	18.01	18.15
55	21.55	21.49	19.96	22.96	20.18	20.68	19.76	22.18	21.50	20.37

TABLE 1.  $U_{10}$  ( $\text{m s}^{-1}$ ).

Fetch (cm)	100	140	160	180	220	260	300	340	380
$U_{10}$ ( $\text{m s}^{-1}$ )									
8.6	0.001	0.001	0.001	0.002	0.005	0.007	0.014	0.02	0.045
13.03	0.004	0.006	0.004	0.009	0.012	0.019	0.022	0.047	0.055
18.15	0.009	0.013	0.011	0.026	0.016	0.019	0.021	0.038	0.050
20.37	0.006	0.010	0.006	0.032	0.013	0.016	0.014	0.062	0.051

TABLE 2. Effective water surface roughness  $z_0$  (cm).

Fetch (cm)	100	140	160	180	220	260	300	340	380	Mean
$U_{10}$ ( $\text{m s}^{-1}$ )										
8.6	0.182	0.213	0.217	0.235	0.254	0.264	0.286	0.297	0.338	0.254
13.03	0.373	0.392	0.356	0.403	0.405	0.425	0.423	0.472	0.478	0.414
18.15	0.543	0.560	0.535	0.617	0.536	0.538	0.531	0.578	0.605	0.560
20.37	0.618	0.640	0.568	0.743	0.610	0.635	0.601	0.759	0.723	0.655

TABLE 3. Friction velocity  $u_*$  ( $\text{m s}^{-1}$ ).

to the point around  $z = 100 \text{ mm}$  (with a possible exception of the shortest fetch,  $x = 100 \text{ cm}$ , where the turbulent boundary layer is probably not fully developed yet, especially at lower flow rates). Therefore, for each vertical distribution of  $U_a(z)$  close to the water surface, a logarithmic curve (4.2) was fitted, and extrapolation to  $z = 10 \text{ m}$  yields corresponding values of  $U_{10}$  (table 1). Values of  $U_{10}$  averaged over all fetches for each prescribed blower speed were chosen as the corresponding representative velocities.

Values of the surface roughness  $z_0$  and friction velocity  $u_*$  were obtained from the fitted logarithmic profiles and are presented in tables 2 and 3, respectively.

The effective water surface roughness showed a general trend of increasing with the fetch and the wind speed, in accordance with waves' amplitude growth.

As expected, the values of  $u_*$  also increase along the test section and under stronger winds. The similarity of the mean normalized logarithmic wind velocity profiles measured at various fetches along the flume and for different wind speed is clearly manifested in figure 4.

The maximum non-dimensional velocity  $U_a/u_*$  in figure 4 is higher at shorter fetches. The decrease of  $U_a/u_*$  with fetch stems both from the slight increase of the friction velocity (table 3) and from the decrease of the mean air velocity due to the small flow rate reduction along the flume. As expected, the thickness of the logarithmic region of the airflow boundary layer grows with the fetch and decreases with the wind flow rate.

The Charnock (1955) parameter  $\alpha_{ch} = z_0 g / u_*^2$  is sometimes used to determine the characteristic surface roughness  $z_0$  by assuming that the values of  $\alpha_{ch}$  are in the range

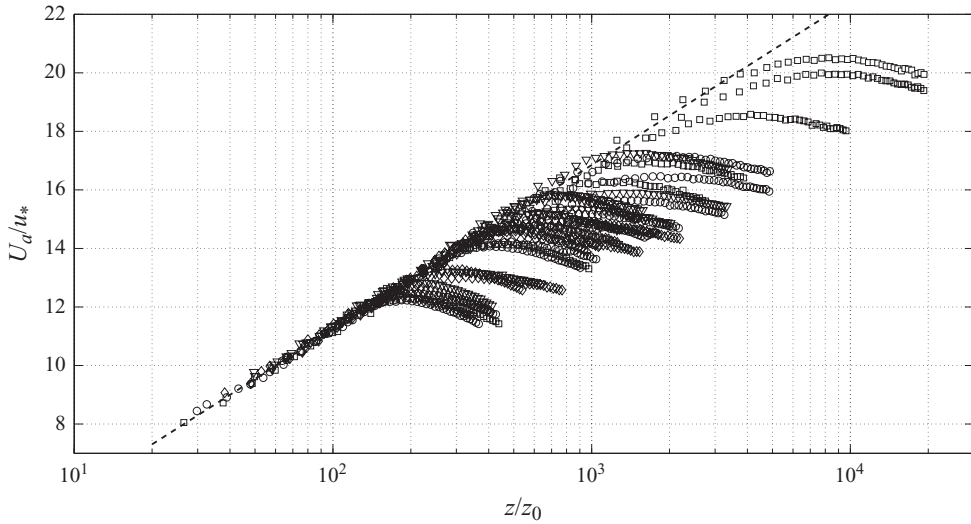


FIGURE 4. Distribution of  $U_d/u_*(z/z_0)$  at various fetches along the flume. Squares,  $U_{10} = 8.6 \text{ m s}^{-1}$ ; circles,  $U_{10} = 13.03 \text{ m s}^{-1}$ ; diamonds,  $U_{10} = 18.15 \text{ m s}^{-1}$ ; triangles,  $U_{10} = 20.37 \text{ m s}^{-1}$ .

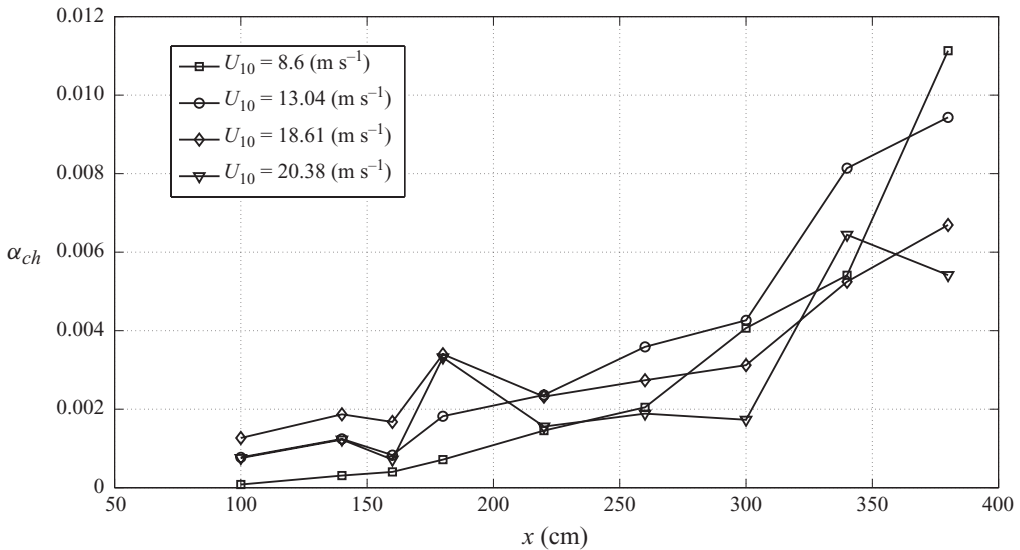


FIGURE 5. Variation of the Charnock parameter  $\alpha_{ch} = z_0 g / u_*^2$  with fetch.

0.01–0.02 ( $\alpha_{ch} = 0.0144$  is a generally accepted value). The values of  $\alpha_{ch}$  calculated using the  $u_*$  and  $z_0$  from tables 2 and 3 are plotted in figure 5.

The values of  $\alpha_{ch}$  in figure 5 are mostly below the generally assumed range with no strong dependence of  $\alpha_{ch}$  on the wind speed; the values of the Charnock parameter in figure 5 increase with  $x$ , approaching the lower limit of the commonly accepted range at fetches that exceed 350 cm.

It is generally accepted that in field measurements, with fetches larger by orders of magnitude, the friction velocity roughly constitutes 5% of  $U_{10}$  (Peirson 1997). The values of  $u_*/U_{10}$  obtained in the present study for fetches exceeding 100 cm are close



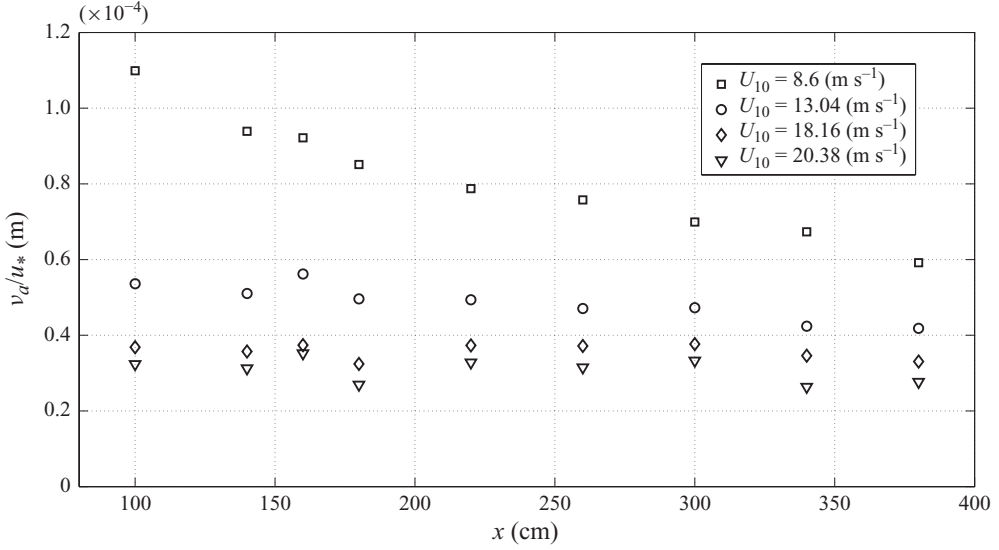


FIGURE 6. Variation of the wall unit  $\nu_a/u_*$  along the flume.

to 3 %, increasing somewhat with fetch and exhibiting no visible dependence on the wind speed.

An additional parameter of interest for the airflow characterization is the ratio between the water surface drift velocity,  $U_s$ , and  $U_{10}$ . Accurate estimates of this parameter from actual measurements are quite difficult, especially in field experiments. In the present study, the determined values of  $U_s/U_{10}$  were around 1.5 % for all four flow rates, somewhat below the generally accepted value of 2 % (Caulliez *et al.* 2008). This slight discrepancy may again stem from the relatively short fetches in the flume.

It is instructive to examine the airflow above the waves in terms of wall parameters. The dimensionless height above the mean water surface in terms of wall units  $\nu_a/u_*$  is

$$z^+ = \frac{z u_*}{\nu_a}, \quad (4.3)$$

$\nu_a$  being the kinematic air viscosity. The distribution of the wall unit  $\nu_a/u_*$  along the test section for four airflow rates is plotted in figure 6. The wall unit values decrease with increase in wind speed and to some extent in fetch, as both the friction velocity and the surface roughness values grow. To further characterize the water surface roughness, it was expressed in terms of wall units as

$$z_0^+ = \frac{z_0 u_*}{\nu_a}, \quad (4.4)$$

in analogy with the notation used for dimensionless roughness characterization for the turbulent flow in rough pipes (Schlichting & Gersten 2000). The distribution of  $z_0^+$  along the flume is presented in figure 7.

For all wind speeds and for fetches up to  $x = 300$  cm, the values of  $z_0^+$  remain below 5, characterizing the flow as smooth according to Schlichting & Gersten (2000). The roughness of the flow then increases with fetch and wind speed; so following the same classification, the airflow in the present study may be characterized as transitionally rough, with  $5 > z_0^+ > 70$  at fetches exceeding  $x = 300$  cm.

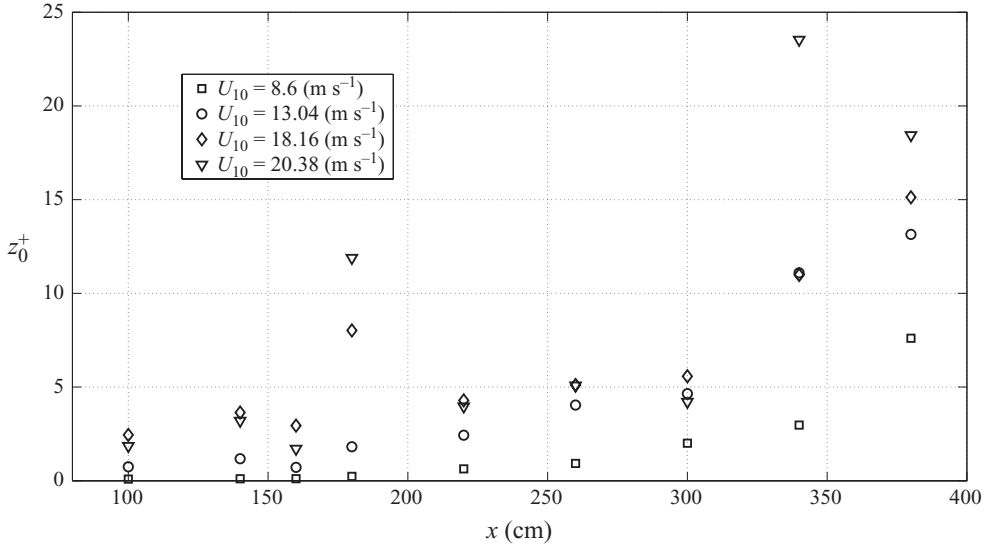


FIGURE 7. Distribution of the dimensionless surface roughness  $z_0^+$  along the flume.

The accuracy of the friction velocity obtained from the mean air velocity profiles measured by the Pitot tube was also examined by independent direct measurements of the vertical profile of the Reynolds stress  $-\overline{u'w'}$ . The total shear stress  $\tau(z)$  in the turbulent airflow above the waves consists of the viscous and Reynolds stresses:

$$\tau = \mu \frac{\partial U_a}{\partial z} - \rho \overline{u'w'}. \quad (4.5)$$

In the logarithmic region, the contribution of the stress due to molecular viscosity is negligible. In the absence of the pressure gradient, the shear stress in boundary flow over a flat surface is constant. In the current experiments, however, pressure variation with  $x$  was detected; the measured pressure drop along the test section is linear, so that  $\partial p / \partial x = \text{const}$  (Liberzon & Shemer 2010). In two-dimensional flow the vertical variation of the shear stress is related to the along-wind pressure gradient by

$$\frac{\partial \tau}{\partial z} = \frac{\partial p}{\partial x} = \text{const}. \quad (4.6)$$

The linear variation of  $-\overline{u'w'}$  with the height above the mean water surface is thus expected. The friction velocity at the water surface can then be estimated as

$$u_* = \lim_{z \rightarrow 0} \sqrt{-\overline{u'w'}}. \quad (4.7)$$

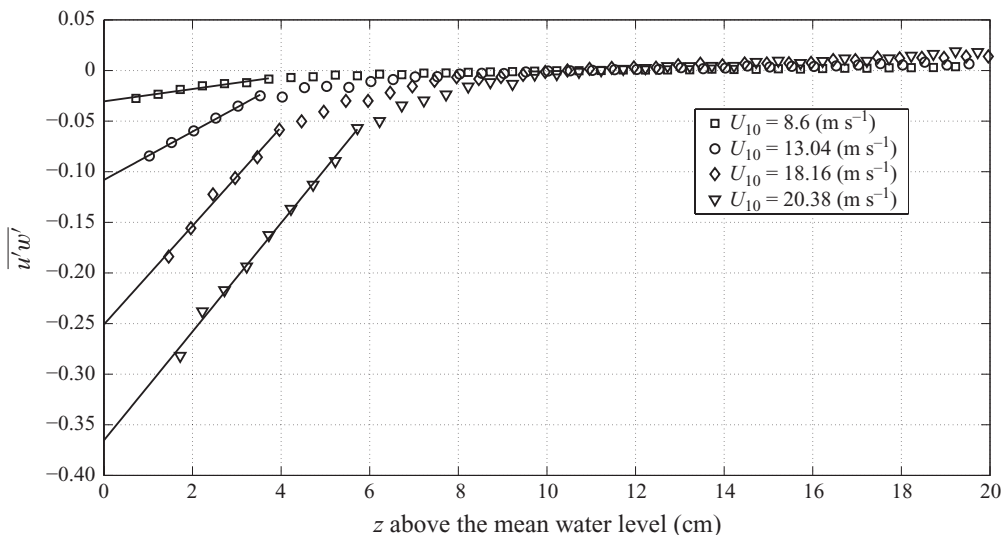
The instantaneous fluctuations of the two air velocity components, the vertical  $w'$  and the horizontal  $u'$ , were measured by a thermoanemometer at  $x = 160$  cm. The obtained vertical distribution of the Reynolds stress  $-\overline{u'w'}$  is presented in figure 8.

The values indeed show linear variation with  $z$  close to the water surface. Extrapolating the linear fit to the water surface at  $z = 0$  yields the shear stress at the interface, see (4.7).

Values of  $u_*$  obtained from the logarithmic mean velocity profiles measured by the Pitot tube and those calculated from the Reynolds stress (table 4) agree for all four airflow rates within about 10 %.

$U_{10}$ (m s <sup>-1</sup> )	$u_*$ (m s <sup>-1</sup> ), Pitot tube	$u_*$ (m s <sup>-1</sup> ), Reynolds stress
8.6	0.22	0.20
13.04	0.36	0.33
18.16	0.54	0.50
20.37	0.57	0.60

TABLE 4. Comparison of independently measured friction velocity values.

FIGURE 8. The distribution of  $-\overline{u'w'}$  above the mean water surface.

This agreement provides additional support for the accuracy of the measurement techniques employed to derive the friction velocity.

#### 4.2. Evolution of wind waves along the test section

The instantaneous surface elevation variation was recorded simultaneously with the airflow measurements for the total duration of 6840 s.

Power spectra of time records were calculated by dividing each record into 30 s windows (corresponding to 4096 data points) with 50 % overlap, resulting in spectral resolution of 0.03 Hz. Representative wave power spectra calculated for each window and then averaged over all 38 records are plotted in figure 9 for each airflow rate at three fetches along the test section.

For each airflow rate, the variation of the spectra with fetch is characterized by an increase in wave energy and a gradual shift towards longer waves with lower frequencies. At any given fetch, the increase in wind flow rate leads to a spectrum dominated by longer waves with lower frequency and higher energy. The dominant frequency for each spectrum was calculated as

$$f_{dom} = \frac{m_1}{m_0}, \quad (4.8)$$

with the  $j$ th spectral moment  $m_j$  of free waves defined as

$$m_j = \int_{\omega_{min}}^{\omega_{max}} \omega^j S(\omega) d\omega. \quad (4.9)$$

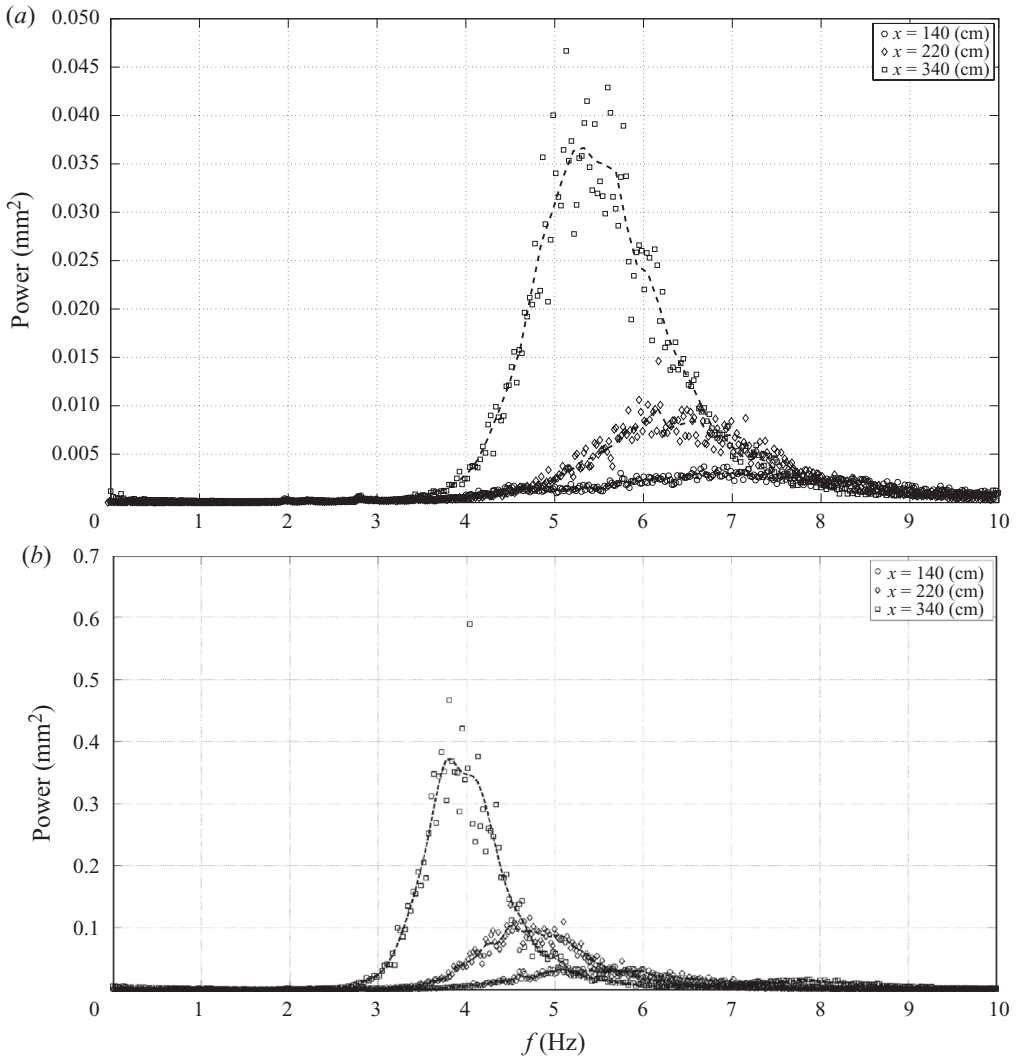


FIGURE 9(a,b). For caption see next page.

Here  $S(\omega)$  is the power spectral component,  $\omega = 2\pi f$  is the radian frequency,  $\omega_{\min}$ ,  $\omega_{\max}$  denote of the limits of the free waves' spectral domain, i.e. only those spectral components which propagate with velocities depending on their own frequencies. A procedure derived by Fedele *et al.* (2010) for wave groups with a narrow spectrum and based on a cubic Schrödinger equation was used to determine the domain limits.

The decrease in dominant frequency with the wind and along the test section is evident in figure 10.

Due to the presence of wind and a water surface drift, the dispersion relation for the gravity–capillary waves does not necessarily hold. The wave phase velocity (celerity) was therefore measured directly using two consecutive probes, and the wavenumber was determined from the independently measured wave celerities and frequencies. Each frequency component of the spectrum was examined separately. Celerity for each frequency was determined by calculating the complex cross-spectrum of the two wave gauges' output. Cross-spectral analysis of two signals  $x(t)$  and  $y(t)$  allows

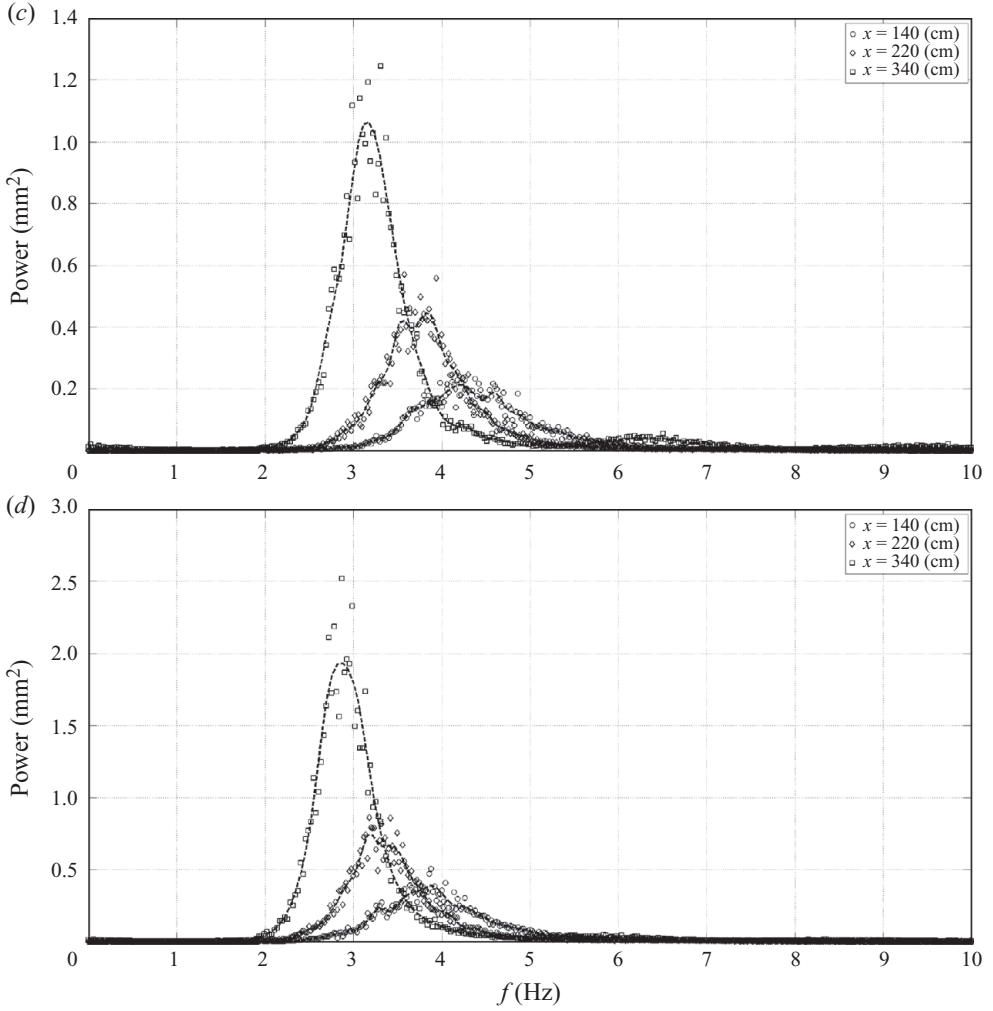
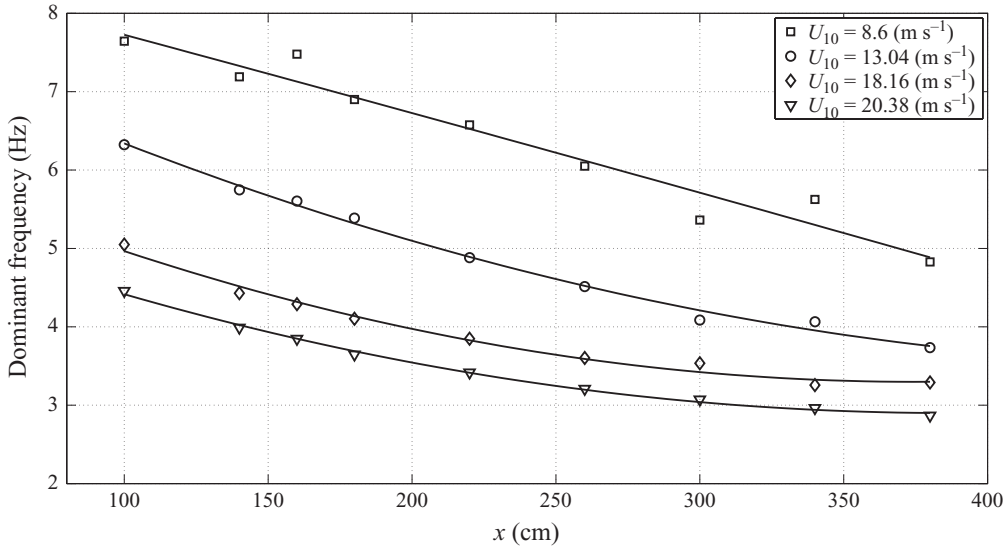
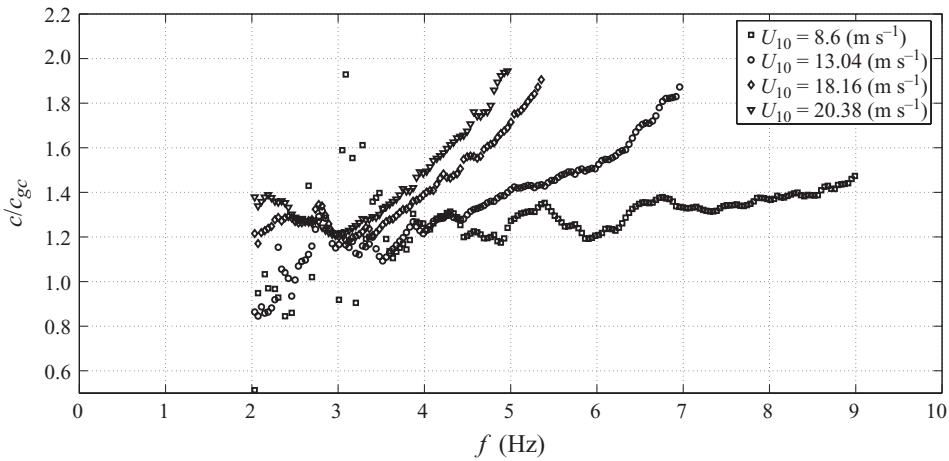


FIGURE 9. Power spectra of the surface elevation. (a)  $U_{10} = 8.6 \text{ m s}^{-1}$ , (b)  $U_{10} = 13.03 \text{ m s}^{-1}$ , (c)  $U_{10} = 18.15 \text{ m s}^{-1}$ , (d)  $U_{10} = 20.37 \text{ m s}^{-1}$ .

determination of the magnitude-squared coherence (MSC) as a function of frequency:

$$\text{MSC}(f) = \frac{|P_{xy}(f)|^2}{P_{xx}(f)P_{yy}(f)}, \quad (4.10)$$

where  $P_{xx}$  and  $P_{yy}$  are the power frequency spectra of each signal, respectively, and  $P_{xy}$  is the complex cross-spectrum (Therrien 1992). At frequencies where the correlation between the signals is significant, the values of MSC are close to unity and become small otherwise. The phase of the cross-spectrum represents the actual phase difference between the two signals at each frequency. Computation of MSC allows one to take into account only those frequency components for which a significant correlation between the two signals exists and thus to decrease the contamination of the results by noise. Detection of the phase lag between the signals from the values of  $P_{\eta_1\eta_2}$  for two consecutive wave gauges allowed determination of the time required for each frequency component to propagate over the distance separating the probes, thus


 FIGURE 10. Variation of the dominant frequency  $f_{dom}$  along the tank.

 FIGURE 11. Dependence of the measured normalized celerities  $c/c_{gc}$  on frequency at  $x = 340$  cm.

enabling calculation of the phase velocity. At each fetch and for each prescribed wind flow rate, the MSC and the cross-spectrum were calculated by averaging over all 38 records. Windows containing 2048 data points each (duration of about 17 s) were used, yielding the frequency resolution of about 0.06 Hz. For each record at a given fetch and airflow rate, the power and the cross-spectra were therefore averaged over 20 windows with a 50 % overlap. Additional details about cross-spectra calculation can be found in Liberzon (2010). The signals were found to be best correlated in the vicinity of the dominant frequency and of its second harmonic. The phase velocity  $c$  was calculated for frequencies at which the MSC exceeds the threshold value of 0.8. The results for a representative fetch  $x = 340$  cm are presented in figure 11. The measured values of  $c$  are normalized in this figure by the celerities  $c_{gc} = \omega/k_{cg}$  at corresponding frequencies  $f = \omega/2\pi$ , with wavenumbers of the gravity-capillary

waves  $k_{cg}$  determined from

$$\omega^2 = gk_{cg} + \frac{\sigma k_{cg}^3}{\rho}, \quad (4.11)$$

where  $\sigma$  is the water–air surface tension.

Relative celerity values tend to decrease first up to frequencies somewhat exceeding the dominant,  $f_{dom}$ , and then increase again towards the second harmonic  $2f_{dom}$ . This increase in  $c$  to values approaching those of the free components around  $f_{dom}$  indicates that the second-order bound waves which propagate with phase velocities of their parent free waves constitute a major contribution to the spectrum at these frequencies.

The measured phase velocities are higher than those expected for gravity–capillary waves at all frequencies due to the Doppler shift, created by the wind-induced shear current in water. The mean water velocity  $U_w(z)$  attains its maximum at the surface and then decays fast. A surface current penetration depth of 900  $\mu\text{m}$  was reported by Banner & Peirson (1998) from direct PIV measurements, while Siddiqui & Loewen (2007), who also applied PIV, report a depth of few millimetres. Direct measurements of both the wave frequency and the celerity allow determination of the corresponding wavenumber

$$k = \frac{\omega}{c}. \quad (4.12)$$

The dominant frequency of the wave field at each of the four airflow rates varies with fetch (see figures 9 and 10). Using the values of  $c$  in the vicinity of  $f_{dom}$  at each fetch, an ensemble of  $c/c_{gc}(k)$  was obtained for all prescribed airflow rates. To obtain the empirical dispersion relation for the free wind waves in the presence of the Doppler shift, a linear curve was fitted to the measured data. The obtained results as well as the empirical dispersion relation of the form

$$\frac{c}{c_{gc}} = 1 + ak + bk^2 \quad (4.13)$$

are presented in figure 12. For comparison, the curve corresponding to the dispersion relation suggested by Choi (1977) in the presence of the wind-induced shear flow,

$$c = U_s - \frac{\lambda U_s}{2k} + \left[ \left( \frac{\lambda U_s}{2k} \right)^2 + \frac{g}{k} + \frac{k\sigma}{\rho_w} \right]^{1/2}, \quad (4.14)$$

is also plotted in figure 12. In (4.14) it is assumed that the water velocity profile is linear:

$$U_w(z) = U_s(1 + \lambda z), \quad (4.15)$$

where

$$\lambda = \frac{r_* u_*^2}{v_w U_s} \quad \text{and} \quad r_* = \frac{\rho_a}{\rho_w}. \quad (4.16)$$

Janssen (1986) showed that for shorter waves,  $k > 1 \text{ cm}^{-1}$ , (4.14) agrees well with the exact results of Kawai (1979) and van Gastel *et al.* (1985).

The Doppler effect due to the wind-induced water current manifests itself in figure 12 as  $c/c_{gc} > 1$  for all wavenumbers. The deviation from the gravity–capillary dispersion relation becomes more pronounced for shorter waves. For the domain of validity of Choi's approximation,  $k > 1 \text{ cm}^{-1}$ , the deviation between (4.14) and the present empirical fit does not exceed a few per cent. Group velocities  $c_{gr}$  were

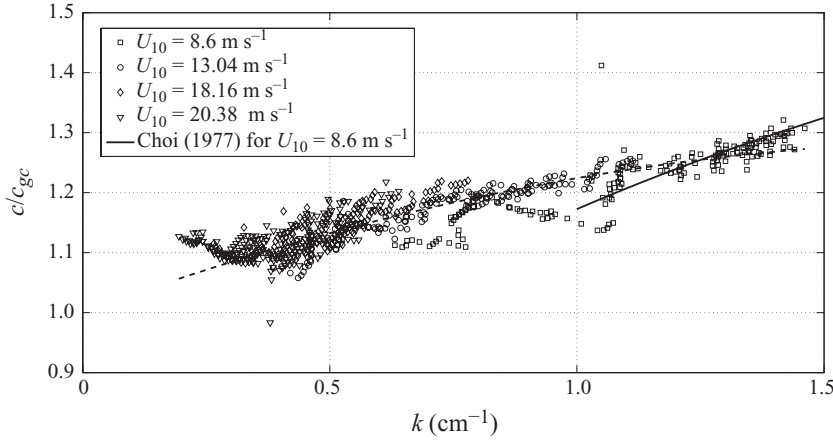


FIGURE 12. Empirical dispersion relation; dashed curve is the fitted empirical dispersion relation ( $a = 0.305$ ,  $b = 0.082$ ).

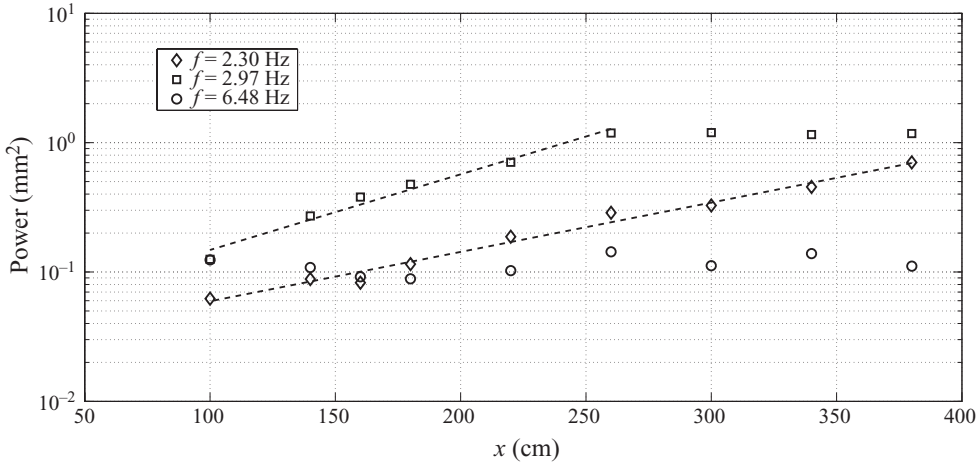


FIGURE 13. Distribution of various frequency components' power along the tank for  $U_{10} = 20.37 \text{ m s}^{-1}$ . Dashed lines denote exponential fit.

calculated using the empirical dispersion relation (4.13):

$$c_{gr} = \frac{\partial \omega}{\partial k} = \frac{\partial}{\partial k} [c_{gc} k (1 + ak + bk^2)]. \quad (4.17)$$

Spatial variation of the spectral power of various frequency components is studied next. Generally speaking, components corresponding to the lower frequencies and thus longer waves show significant growth, while components at frequencies exceeding about 6 Hz generally retain their amplitude along the flume. To estimate the growth of energetic components along the test section, some representative results on the spatial variation of their power are plotted in figure 13. The power of some components increases along the whole test section ( $f = 2.3 \text{ Hz}$ ), while at other frequencies the wave power grows up to a specific fetch and then remains virtually constant at more distant fetches ( $f = 2.97 \text{ Hz}$ ). The exponential fit of the form

$$a_f^2 = a_{f,0}^2 \exp(\gamma x), \quad (4.18)$$



with  $a_{f,0}$  being the initial wave's component power allows determination of the spatial growth rate  $\gamma$ .

#### 4.3. Wind–waves momentum transfer

Surface undulations due to waves induce pressure fluctuations  $p'$  in the air. The measured pressure fluctuations thus result from both the free-stream turbulence and the surface-induced contributions. In potential flow over an undulating surface, the induced pressure fluctuations are  $180^\circ$  out of phase with the surface elevation ( $\theta_p = \pi$ ), while the amplitudes decrease exponentially with height as  $e^{-kz}$ , with  $k$  being the wavenumber of the corresponding wave component (Young 1999). Although there is a considerable similarity between the airflow over the propagating water waves and that over a sinusoidally shaped plate moving at a speed corresponding to the waves' phase velocity, significant differences exist. Contrary to the moving rigid plate case, the water surface and the waves' parameters do not remain constant as waves evolve with fetch. On-surface pressure fluctuations constitute the major mechanism by which momentum can be transferred from the airflow to the water waves; hence, evaluation of amplitudes of the wave-induced static pressure fluctuations at the mean water surface and of the pressure fluctuations phase relative to the surface elevation is of paramount importance for the momentum transfer estimation. The goal of the current study of the initial stages of waves' excitation by wind corresponds to very young sea conditions with the wave age values in the range  $0.01 > c/u_* > 1.5$ . The amount of work being done by pressure on the water surface is given by

$$\frac{\partial E(\omega)}{\partial t} = \frac{1}{\rho_w g} \tau_{form} \frac{1}{2} c, \quad (4.19)$$

where  $E(\omega)$  is the one-dimensional power spectrum of surface elevation and  $\tau_{form}$  is the form drag (Donelan *et al.* 1999; Young 1999; Jansen 2004). Averaging over the dominant wavelength  $\lambda_0$ , the form drag due to the pressure fluctuations amplitudes on the mean surface,  $p_0$ , is defined as

$$\tau_{form} = \overline{p_0 \frac{\partial \eta}{\partial x}} = -\frac{1}{\lambda_0} \int_0^{2\pi/k_0} p_0 \frac{\partial \eta}{\partial x} dx, \quad (4.20)$$

where the overbar represents averaging with respect to time. In the linear approximation, for each frequency harmonic (4.20) yields

$$\tau_{form} = \frac{\omega_0 \eta_0 p_0}{2c} \sin(\theta_p). \quad (4.21)$$

To estimate the values of  $p_0$  and  $\theta_p$  as accurately as possible, static pressure fluctuations were recorded simultaneously with the surface elevation and the air velocity measurements at all heights above the waves. Note that measurements of pressure fluctuations are less accurate than those of the surface elevation for two reasons. First, the fluctuations of pressure contain, in addition to the coherent contribution resulting from water surface undulations, also a random component due to the background turbulent flow. Second, at each vertical location only relatively short, 3 min long, pressure records are available, as opposed to nearly 2 h long cumulative wave records.

To get a better understanding of the relative importance of the coherent part of the pressure fluctuations, the MSC values for surface elevation and pressure fluctuations were calculated from the accumulated records. The surface elevation  $\eta$  and the static pressure  $p$  cross-spectra  $P_{\eta p}$  and the corresponding MSC values were calculated by

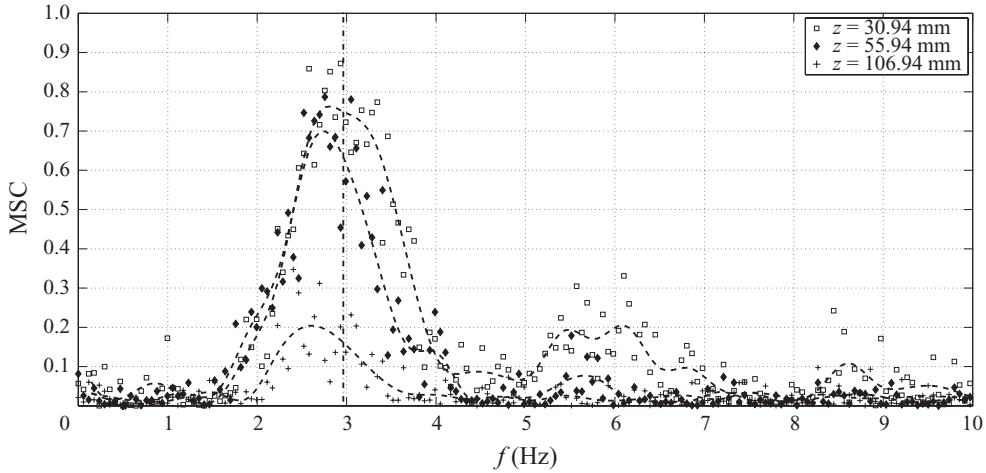


FIGURE 14. Magnitude-squared coherence between the static pressure fluctuations at various heights and the surface elevation variations for  $U_{10} = 20.37 \text{ m s}^{-1}$  at  $x = 340 \text{ cm}$ . The vertical dash-dotted line represents the dominant frequency of surface waves.

dividing each record into windows containing 4096 points (duration of about 30 s) with a 50 % overlap, resulting in a 0.03 Hz spectral resolution. Some representative results of the MSC dependence on frequency are given in figure 14.

The MSC values are generally quite small, the correlation between surface elevation and pressure variations becoming significant mainly close to the air–water interface and in the vicinity of the dominant wave frequency  $f_{dom}$ . The variation of the MSC with the frequency strongly resembles that of the wave frequency spectrum (figure 9); at the lowest heights significant correlation seems to exist also at frequencies corresponding to the second, and to some extent, even to the third harmonic of  $f_{dom}$ . Such behaviour clearly demonstrates that the coherent free- and bound-wave-related contribution to the static pressure fluctuations in the turbulent airflow indeed becomes dominant under those conditions.

Representative power spectra  $P_p(f)$  of time records of the static pressure fluctuations are presented in figure 15.

The wave-related contribution is of the main interest here as it is instrumental in the wind–wave momentum transfer. For all cases examined, considerable static pressure fluctuations were detected mainly at conditions corresponding to a significant correlation between the pressure and the surface elevation. For any given fetch and wind speed, the amplitude of the pressure fluctuations decreases with height, and no pressure fluctuations of considerable power were detected at higher vertical locations. It thus can be deduced that the pressure fluctuations measured in the vicinity of the water surface at stronger winds are mainly wave-induced, while the fluctuations contributed by the background flow turbulence at those heights are relatively minor. This conclusion also agrees well with the results of numerical simulations by Sullivan, McWilliams & Moeng (2000). For the air flowing at a relatively low Reynolds number over monochromatic waves with wavenumber  $k$ , they showed that wave-induced pressure fluctuations are noticeable at elevations satisfying  $kz < 1$ .

The root-mean-square (r.m.s.) values of the pressure fluctuations in each record were therefore used as characterizing pressure fluctuation amplitudes. For all flow rates, the r.m.s. values of the static pressure fluctuations at vertical locations close

Fetch (cm)	100	140	160	180	220	260	300	340	380
$U_{10}$ (m s <sup>-1</sup> )									
8.6	0.054	0.041	0.079	0.013	0.020	0.128	0.120	0.088	0.111
13.03	0.150	0.236	0.172	0.137	0.154	0.194	0.201	0.226	0.250
18.15	0.229	0.270	0.266	0.467	0.543	0.548	0.508	0.596	0.452
20.37	0.343	0.402	0.487	0.629	0.637	0.809	0.829	0.939	0.710

TABLE 5. Pressure decay coefficient  $\alpha$ .

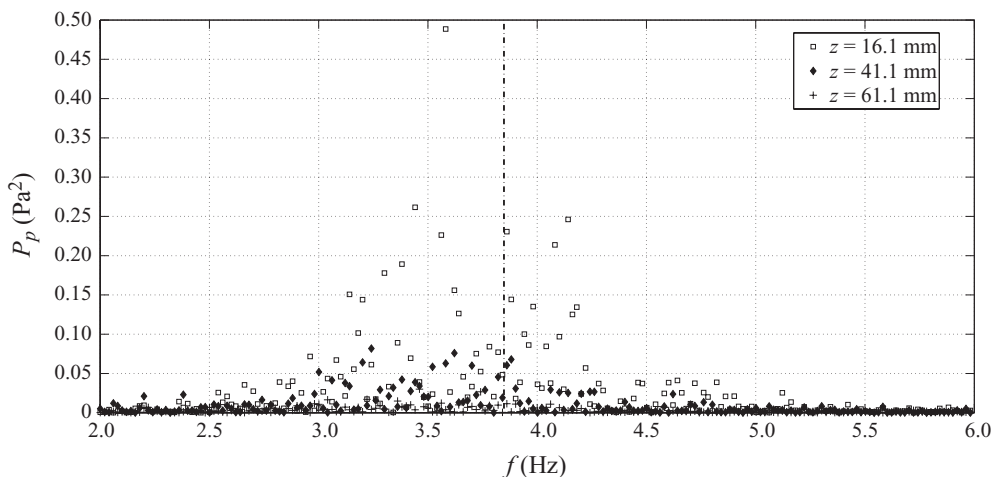


FIGURE 15. Static pressure fluctuation power spectra at various heights above the mean water surface at  $x = 340$  cm and  $U_{10} = 20.37$  m s<sup>-1</sup>. The vertical dashed-dotted line represents the dominant frequency of surface waves.

to the interface were found to decay with  $z$  (with a possible exception of the lowest airflow rate where no waves of considerable amplitude were excited). The decay rates were evaluated using an exponential fit, with the dominant wavenumber at the appropriate experimental condition,  $k_0$ , estimated from the empirical dispersion relation (see figure 12), serving as the scaling parameter

$$p(k_0 z) = p_0 \exp(-\alpha k_0 z). \quad (4.22)$$

Here  $p_0$  is the characteristic static pressure fluctuation amplitude evaluated at the mean water surface ( $z=0$ ) and  $\alpha$  is the dimensionless pressure decay rate. Vertical distributions of static pressure r.m.s. values with the corresponding fit curves are presented in figure 16 at three representative fetches for four prescribed wind velocities.

The decay rate coefficients  $\alpha$  derived from the exponential fit curves are summarized in table 5.

All values of  $\alpha$  in table 5 are smaller than unity that corresponds to the potential flow, while increase in fetch and/or in wind speed leads to increase in  $\alpha$ . The deviation from the potential flow solution is in good qualitative agreement with field measurements of Hare *et al.* (1997) and with the laboratory study of Mastenbroek *et al.* (1996), in which the pressure decay coefficients  $\alpha < 1$  were reported for some of the cases examined. Both these studies dealt with intermediate and mature seas,

Fetch (cm)	100	140	160	180	220	260	300	340	380
$U_{10}$ (m s <sup>-1</sup> )									
8.6	0.43	0.38	0.35	0.32	0.33	0.40	0.49	0.57	0.78
13.03	1.05	1.34	1.07	1.15	1.19	1.33	1.60	1.93	2.20
18.15	2.78	3.23	3.19	4.07	4.29	4.66	4.72	5.57	5.30
20.37	4.90	6.54	7.57	9.56	8.74	9.64	10.18	14.21	11.26

TABLE 6. Amplitudes of static pressure fluctuations at water surface,  $p_0$  (Pa).

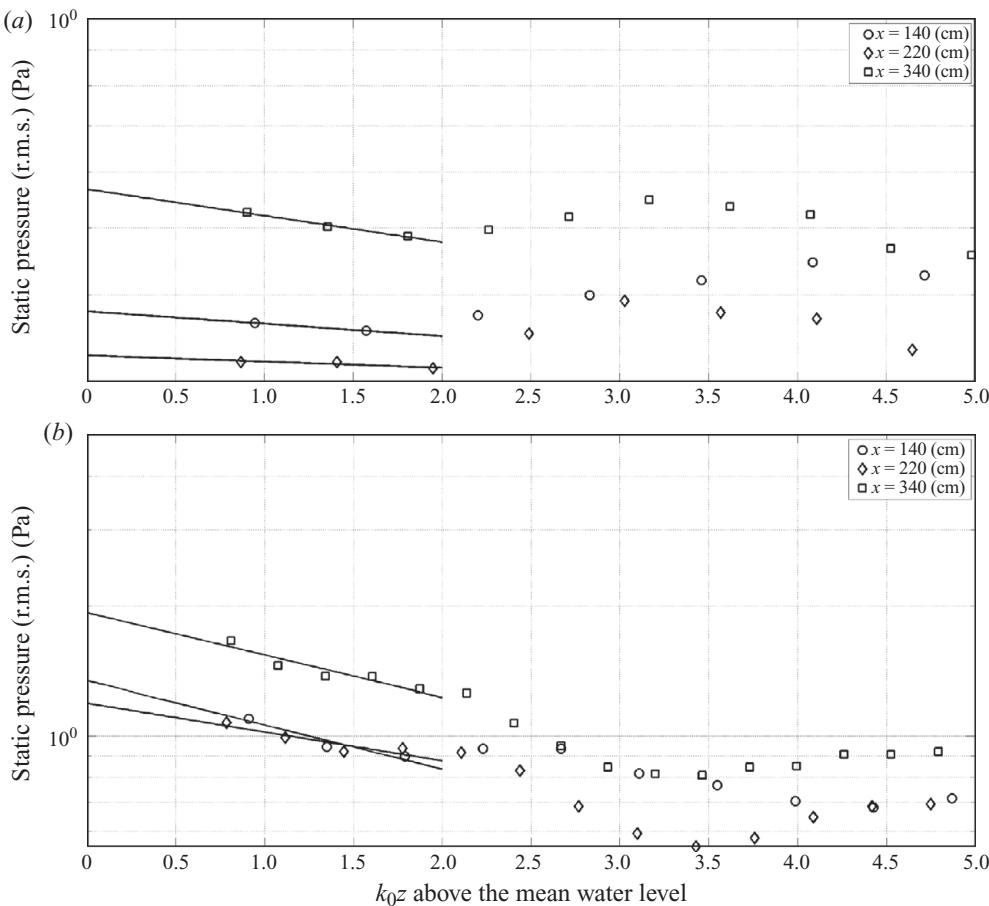


FIGURE 16(a,b). For caption see next page.

$c/u_* > 2.4$ , as compared to much younger sea conditions in the present study, thus preventing quantitative comparison.

The amplitudes of pressure fluctuations at the mean water surface were obtained extrapolating the fitted curves (figure 16) to  $z=0$ , so that  $p_0 = \sqrt{2}p(z_0)$ . The values of  $p_0$  are summarized in table 6.

The amplitude of the surface pressure fluctuations increases with fetch and wind speed, remaining in the range of a few Pa. These values of  $p_0$  are in a qualitative agreement with measurements by Donelan *et al.* (2006), and in good quantitative

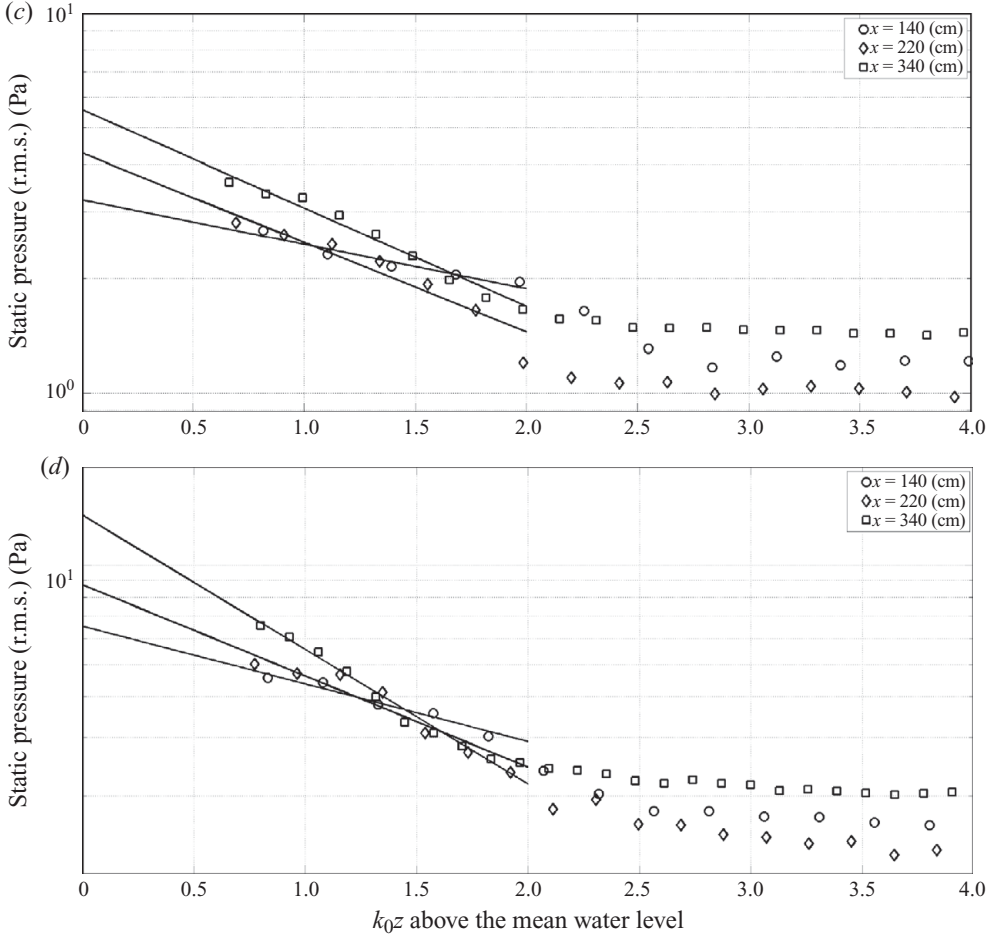


FIGURE 16. The decay of the r.m.s. values of the static pressure with height. (a)  $U_{10} = 8.6 \text{ m s}^{-1}$ , (b)  $U_{10} = 13.03 \text{ m s}^{-1}$ , (c)  $U_{10} = 18.15 \text{ m s}^{-1}$ , (d)  $U_{10} = 20.37 \text{ m s}^{-1}$ .

agreement with the results of Hare *et al.* (1997), in spite of the different range ( $2.5 < c/u_* < 10$ ) of wave ages considered in those investigations.

The phase differences between the pressure fluctuations and the surface elevation were obtained from the complex cross-spectra  $P_{\eta p}(f)$  only for frequencies at which significant correlation was detected (defined as  $\text{MSC} > 0.6$ ). Distributions of  $\theta_p$  with the frequency at various heights for a number of cases are presented in figure 17.

For all experimental conditions at which significant correlation between pressure and surface elevation fluctuations was detected, the values of  $\theta_p$  were smaller than  $180^\circ$  and showed no notable variations with  $z$ . These phase angles of pressure fluctuations are in good agreement with the results reported by Hare *et al.* (1997), Mastenbroek *et al.* (1996) and Donelan *et al.* (2006). Hence, the representative values of  $\theta_p$  used to evaluate the form drag from (4.21) were obtained by averaging the measured phases over all heights.

The total shear stress  $\tau_{\text{total}}$  near the water surface has contributions from a viscous stress and a form drag,

$$\tau_{\text{total}} = \rho_a u_*^2 = \tau_{\text{visc}} + \tau_{\text{form}}. \quad (4.23)$$

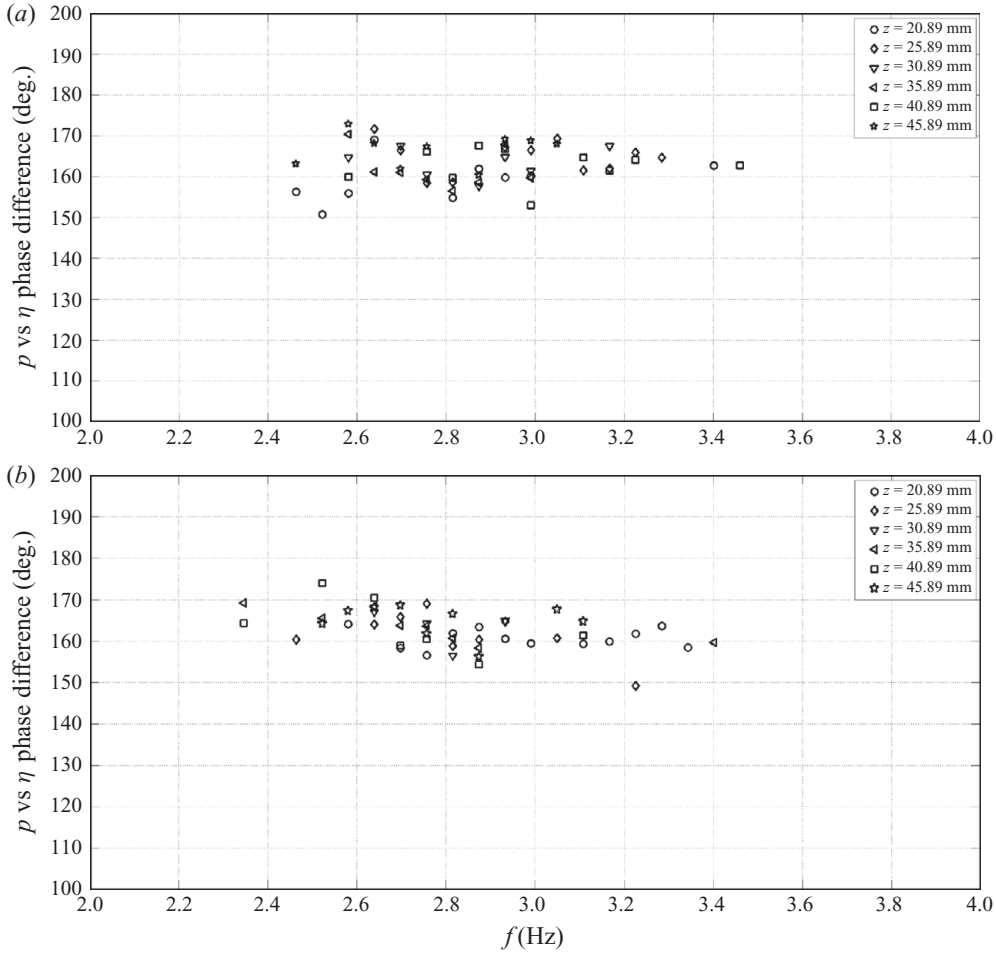


FIGURE 17. Phase difference between static pressure and surface elevation variations for various frequencies for  $U_{10} = 20.37 \text{ m s}^{-1}$  at (a)  $x = 300 \text{ cm}$  and (b)  $x = 340 \text{ cm}$ .

The values of  $\tau_{\text{visc}}$  and  $\tau_{\text{form}}$  calculated from (4.21) and (4.23) are compared for all experimental conditions in figure 18.

Figure 18(a) shows  $\tau_{\text{total}}$  versus  $\tau_{\text{form}}$  on a log-log scale, while the ratio  $\tau_{\text{form}}/\tau_{\text{total}}$  as a function of fetch is presented figure 18(b).

For the whole range of experimental parameters in this study, values of  $\tau_{\text{form}}$  remain below 1 Pa. The role of viscous stress decreases significantly as the sea matures over the whole range of experimental conditions studied. That observation agrees well with the widely accepted assumption of negligible contribution of viscous stress to the total shear stress for mature sea conditions (Janssen & Lionello 1989; Drennan *et al.* 1999; Makin & Kudryavtsev 2002).

The obtained values of the form drag were used to evaluate the spatial growth rate of the waves. The temporal growth rate of a component with the radian frequency  $\omega = 2\pi f$  can be expressed in terms of energy flux (4.19) as

$$\beta = \frac{1}{E(\omega)} \frac{\partial E(\omega)}{\partial t} = \frac{1}{\rho_w g} \frac{\omega_0 \eta_0 p_0}{4 \langle \eta \rangle^2} \sin(\theta_p). \quad (4.24)$$

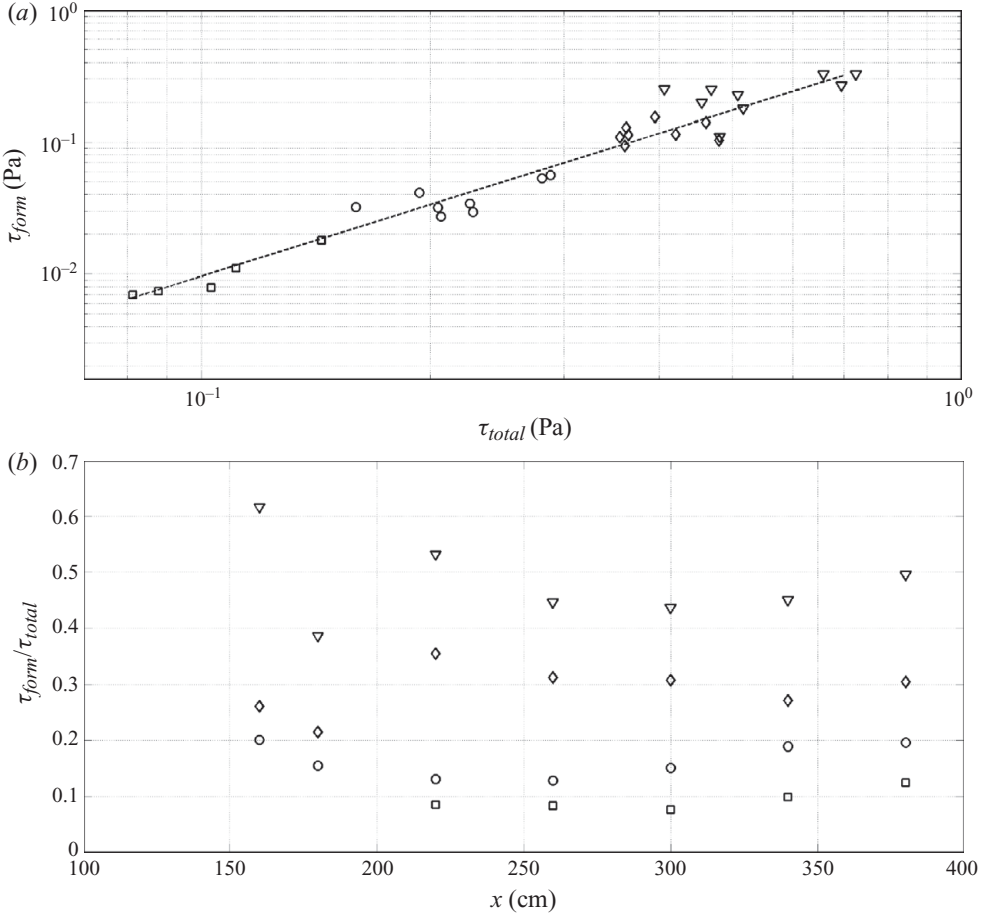


FIGURE 18. (a) Values of total stress and form drag at various fetches for four prescribed wind velocities. (b) Distribution of the  $\tau_{form}/\tau_{total}$  ratio along the flume. Squares,  $U_{10} = 8.6 \text{ m s}^{-1}$ ; circles,  $U_{10} = 13.03 \text{ m s}^{-1}$ ; diamonds,  $U_{10} = 18.15 \text{ m s}^{-1}$ ; triangles,  $U_{10} = 20.37 \text{ m s}^{-1}$ .

The spatial growth rate that can be directly measured in the present experiments is then obtained from (4.24), invoking group velocity values  $c_{gr}$  calculated using (4.17),

$$\gamma = \frac{1}{\rho_w g} \frac{\omega_0 \eta_0 p_0}{4 \langle \eta \rangle^2 c_{gr}} \sin(\theta_p). \quad (4.25)$$

Data accumulated in the present study make it possible to carry out a comparison of the directly determined growth rates for waves of various frequencies in the vicinity of the dominant frequency for each prescribed flow rate with those calculated from the energy flux estimation. The fit of both field and laboratory experiments compiled by Plant (1982) yielded the following relation for waves propagating in the direction of the mean wind:

$$\frac{\beta}{\omega} = (0.04 \pm 50 \%) \frac{u_*^2}{c^2}. \quad (4.26)$$

To compare our results with the empirical fit (4.26), the spatial growth rate  $\gamma$  is obtained from  $\beta$  again invoking  $c_{gr}$  based on the empirical dispersion relation (4.17).

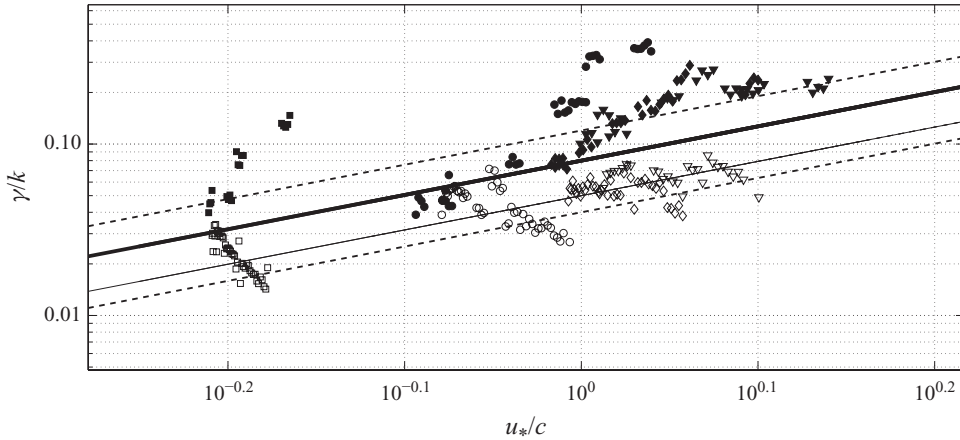


FIGURE 19. Dimensionless spatial wave energy growth rates. Squares,  $U_{10} = 8.6 \text{ (m s}^{-1}\text{)}$ ; circles,  $U_{10} = 13.03 \text{ (m s}^{-1}\text{)}$ ; diamonds,  $U_{10} = 18.15 \text{ (m s}^{-1}\text{)}$ ; triangles,  $U_{10} = 20.37 \text{ (m s}^{-1}\text{)}$ . Empty and filled markers denote values determined by direct examination of the evolution along the flume of each frequency component and those obtained by momentum flux estimates (4.25), respectively. Thick solid line and the dashed lines correspond to the empirical relation (4.26) with confidence intervals. Thin solid line denotes estimates by Miles (1959).

In figure 19, the directly measured values of the dimensional spatial growth rate  $\gamma$  based on the exponential fit (figure 13) are juxtaposed with those estimated from the energy flux evaluation. Curves corresponding to the empirical relation (4.26) are plotted as well.

Strict criteria were applied to ensure data accuracy in estimating the directly measured values of  $\gamma$ . Only those frequency components at which clear exponential growth with a constant rate was observed along at least three examined fetches were taken into account. In cases where the spatial growth pattern was followed by a saturation (as in figure 13 for  $f = 2.97 \text{ Hz}$ ), the fetch at which the inception of saturation was detected was excluded from the calculations.

## 5. Discussion and summary

According to the shear flow model, the rate of energy transfer from wind to waves is proportional to the wind profile curvature  $U''(z_{cr})$  at the critical height, where the wind speed equals the phase velocity of the wave,  $U(z_{cr}) = c$ . The celerity  $c$  of the dominant wave can be determined from the empirical dispersion relation (figure 12), and thus the critical-layer thickness  $z_{cr}$  can be evaluated. The wave age of dominant waves in the present study that can be seen as the mean velocity in wall units at the critical-layer height,  $u^+(z_{cr}) = c/u^*$ , does not exceed 1.6 (see figure 19). The critical layer is thus situated deep inside the viscous sublayer that extends to about  $z^+ = 5$  and characterized by the velocity profile  $u^+ = z^+$  (Shlichting & Gersten 2000). No curvature in the air velocity profile is therefore supposed to exist in such a proximity to the interface. All vertical coordinates in this study were calculated relative to the mean water surface. Taking into account the prevailing wave heights, the critical layer in the present experiments is mostly below waves' crests. Imposing the airflow boundary conditions at the moving curved water surface rather than at the mean water level was indeed considered by Miles (1959) and Reutov & Troitskaya (1996).



Miles (1959) indicated that this modification does not change the results considerably. More accurate measurements of the pressure fluctuations in the immediate vicinity of the moving interface require not only positioning of the probe on a floating platform, but also probe's spatial resolution of the order of a wall unit, i.e. ranging from 10 to 100  $\mu\text{m}$ , much smaller than the size of presently available sensors.

The results on distribution of the critical-layer thickness, together with the detected exponential growth of waves at various frequencies, raise a fundamental question about the validity of the shear flow model for describing the initial stages of water waves' excitation by wind for young sea with  $z_{cr}^+ = O(1)$ . The inability of Miles' critical-layer mechanism to serve as the important factor in the growth of slowly propagating short waves has already been discussed in the literature, see e.g. Peirson & Garcia (2008). The situation may be different for the mature sea conditions, for which the applicability of the model received some support from relatively recent field experiments (Hristov *et al.* 2003). The lack of suitable instrumentation also prevents quantitative validation of the Phillips (1957) resonant theory.

In summary, an extensive set of experimental data on the initial stages of water waves' excitation by wind is presented in this study. The measured vertical profiles of the mean airflow velocity at nine fetches and four prescribed flow rates enabled determination of the variation along the test section of both the friction velocity  $u_*$  and the characteristic roughness of the water surface  $z_0$ . For a given airflow rate, the friction velocity  $u_*$  does not vary significantly along the tank. Fluctuations of the vertical and the horizontal airflow velocity components were also measured and used to validate the accuracy of the Pitot tube derived values of  $u_*$ . The extrapolated, to the mean water surface level, measured vertical profiles of the time-averaged turbulent Reynolds stress were compared with the Pitot tube derived values of  $u_*^2$ . Extrapolation of the logarithmic velocity profile to  $z = 10\text{ m}$  was used to determine the characteristic wind velocity  $U_{10}$ . An analysis of wind velocity profiles in view of the boundary-layer theory was also performed and dimensionless parameters such as the ratios between the characteristic wind velocities  $U_{10}$  and  $u_*$  and the water surface drift velocity, surface roughness and the critical-layer thickness in wall units are presented. A cross-spectral analysis was used extensively to determine relations between various flow parameters. The value of the MSC was used to filter out unreliable data. Simultaneously with the measurements of the airflow, at any given fetch and airflow rate, the instantaneous water surface elevation variation was recorded by two consecutive wave gauges at a prescribed distance, thus making possible a direct determination of celerities of various wave frequency harmonics. An empirical dispersion relation was then obtained to determine the actual, modified by the Doppler effect, wavelengths at various frequencies.

Evolution of the wind-wave spectra along the tank was studied for all airflow rates considered. Dominant frequencies were determined for each fetch and wind speed using the integral moments of the power spectrum of the surface elevation. Downshifting of the dominant frequency with fetch and the wind speed was documented. The spatial variation of the amplitude of various frequency harmonics was obtained. For certain ranges of frequencies and fetches, an exponential growth was observed, enabling determination of the spatial growth rate for each one of those frequency components.

Direct measurements of the spatial growth rates of waves' components of various frequencies were carried out together with the evaluation of a corresponding wind to waves momentum transfer. Extensive and relatively accurate measurements of the static pressure fluctuations with a reasonable spatial resolution reported here became

possible due to application of a commercially available pressure sensor (Liberzon & Shemer 2010). Nevertheless, pressure variation amplitudes at the water surface had to be estimated by extrapolating the exponentially decaying values measured higher above the waves. The accuracy of this method is somewhat questionable although it was widely used in numerous studies (e.g. Snyder 1974; Papadimitrakis *et al.* 1986; Mastenbroek *et al.* 1996; Donelan *et al.* 2006). The pressure fluctuation values in the present study were obtained at numerous vertical locations as compared to just a few vertical positions in Snyder (1974) and Hare *et al.* (1997). These detailed measurements allowed a more accurate exponential fit to estimate the pressure amplitude at the air–water interface,  $p_0$ . The results of Donelan *et al.* (2005, 2006) obtained for the intermediate and mature seas suggest that the pressure decay rate  $\alpha$  increases with wave age. The values of  $\alpha < 1$  reported in the present study for young sea conditions corroborate that suggestion. Spectra of static pressure fluctuations at various heights above the mean water surface were obtained for all fetches and wind speeds. Away from the interface, the measured amplitudes of the pressure fluctuations were usually negligibly small and spread over a wide range of frequencies. Closer to the air–water interface, the amplitude of the static pressure fluctuations increased considerably and the frequency spectrum exhibited a close resemblance to that of surface elevation, with a strong peak around the waves' dominant frequency. The similarity between the spectra of pressure fluctuations and the surface elevation in the vicinity of the interface suggested strong correlation between the two signals. The cross-spectral analysis of the surface elevation and the static pressure variation in time was carried out. The phase of the pressure–surface elevation cross-spectrum was determined for those conditions where the MSC of the two signals is sufficiently high. The phase lag of the pressure relative to the surface elevation in all cases did not vary significantly with height, always remaining below  $\theta_p = 180^\circ$  and thus indicating the existence of energy flux from wind to waves. The measured values of the phase lag and the estimates of pressure oscillations amplitude at the mean air–water interface were used to evaluate the form drag. The dependence of the form drag on fetch and the wind velocity was obtained and compared with the measured viscous drag. Experimentally determined form drag values enabled calculation of the spatial wave growth rate due to wind energy input. To compare these values with the directly obtained spatial growth rates, both parameters were presented as functions of the inverse wave age  $u_*/c$  (figure 19). Comparison was also carried out with an empirical relation based on the compilation of the available data by Plant (1982), as well as with theoretical predictions.

For all experimental conditions, spatial growth rates based on the momentum transfer were found to exceed those obtained by direct determination of the increase of wave amplitudes with fetch. The disagreement of the directly determined spatial growth rates with the previously available data and those predicted theoretically by the shear flow model decreases as the characteristic wavelength increases. This result can be attributed to viscous dissipation, wave breaking and nonlinear interactions among waves.

Support of this study by grant 1194/07 from the Israeli Science Foundation is gratefully acknowledged.

## REFERENCES

- AGNON Y., BABANIN, A. V., YOUNG, I. R. & CHALIKOV, D. 2005 Fine scale inhomogeneity of wind–wave energy input, skewness, and asymmetry. *Geophys. Res. Lett.* **32**, L12603.

- ATHANASSIADOU, M. 2003 Wave and form drag: their relation in the linear gravity wave regime. *Tellus* **55A**, 173–180.
- BANNER, M. L. & PEIRSON, W. L. 1998 Tangential stress beneath wind-driven air–water interface. *J. Fluid Mech.* **364**, 115–145.
- BELCHER, S. E. & HUNT, J. C. R. 1998 Turbulent flow over hills and waves. *Annu. Rev. Fluid Mech.* **30**, 507–538.
- BELCHER, S. E. & WOOD, N. 1996 Form and wave drag due to stably stratified turbulent flow over low ridges. *Q. J. R. Meteorol. Soc.* **122**, 863–902.
- BENJAMIN, T. B. 1959 Shearing flow over a wavy boundary. *J. Fluid Mech.* **6**, 161–205.
- CAULLIEZ, G., MAKIN, V. & KUDRYAVTSEV, V. 2008 Drag of the water surface at very short fetches: observations and modeling. *J. Phys. Oceanogr.* **38**, 2038–2055.
- CAULLIEZ, G., RICCI, N. & DUPONT, R. 1998 The generation of the first visible wind waves. *Phys. Fluids* **10** (4), 757–759.
- CHAPMAN, R. & MONALDO, F. M. 1995 A novel wave height sensor. *J. Atmos. Ocean. Technol.* **12**, 190–196.
- CHARNOCK, H. 1955 Wind stress on water surface. *Q. J. R. Meteorol. Soc.* **81**, 639–640.
- CHOI, I. 1977 Contributions à l'étude des mécanismes physiques de la génération des ondes de capillarité-gravité à une interface air-eau. Thesis, Université d'Aix Marseille.
- CONTE, S. D. & MILES, J. W. 1959 On the integration of Orr–Sommerfeld equation. *J. Soc. Ind. Appl. Maths* **7**, 361–369.
- DONELAN, M. A., BABANIN, A. V., YOUNG, I. R. & BANNER, M. L. 2006 Wave-follower field, measurements of the wind-input spectral function. Part II. Parameterization of wind input. *J. Phys. Oceanogr.* **36**, 1672–1689.
- DONELAN, M. A., BABANIN, A. V., YOUNG, I. R., BANNER, M. L. & MCCORMICK, C. 2005 Wave-follower field measurements of the wind-input spectral function. Part I. Measurements and calibrations. *J. Atmos. Ocean. Technol.* **22**, 799–813.
- DONELAN, M. A., MADSEN, N., KAHMA, K. K., TSANIS, I. K. & DRENNAN, W. M. 1999 Apparatus for atmospheric surface layer measurements over waves. *J. Atmos. Ocean. Technol.* **16**, 1172–1182.
- DRENNAN, W., KIMMO, K., KAHMA, K. K. & DONELAN, M. A. 1999 On momentum flux and velocity spectra over waves. *Boundary-Layer Meteorol.* **92** (3), 489–515.
- ELLIOTT, J. A. 1972 Instrumentation for measuring static pressure fluctuations within the atmospheric boundary layer. *Boundary-Layer Meteorol.* **22**, 476–495.
- FEDELE, F., CHERNEVA, Z., TAYFUN, M. A. & GUEDES SOARES, C. 2010 Nonlinear Schrödinger invariants and wave statistics. *Phys. Fluids* **22**, 036601.
- VAN GASTEL, K., JANSSEN, P. A. E. M. & KOMEN, G. J. 1985 On phase velocity and growth rate of wind-induced gravity–capillary waves. *J. Fluid Mech.* **161**, 199–216.
- GILL, G. C. 1976 Development and testing of a non-moving-parts static pressure inlet for use on ocean buoys. *University of Michigan Rep.*, NOAA 01-6-038-115, 43 pp.
- HARE, J. E., HARA, T., EDSON, J. B. & WILCZAK, J. M. 1997 A similarity analysis of the structure of airflow over surface waves. *J. Phys. Oceanogr.* **27**, 1018–1037.
- HERRING, F., LEUE, C., WIERZIMOK, D. & JANHE, B. 1998 Particle tracking velocimetry beneath water waves. Part II. Water waves. *Exp. Fluids* **24**, 10.
- HRISTOV, T. S., MILLER, S. D. & FRIEHE, C. A. 2003 Dynamic coupling of wind and ocean waves through wave-induced air flow. *Nature* **442**, 55–58.
- HSU, C. T. & HSU, E. Y. 1983 On the structure of turbulent flow over a progressive water wave: theory and experiments on a transformed wave-following coordinate system. Part 2. *J. Fluid Mech.* **131**, 123–153.
- JANSSEN, P. A. E. M. 1986 The period-doubling of gravity–capillary waves. *J. Fluid Mech.* **172**, 531–546.
- JANSSEN, P. A. E. M. 1989 Wave-induced stress and drag of air flow over sea waves. *J. Phys. Oceanogr.* **19**, 745–754.
- JANSSEN, P. A. E. M. 2004 *The Interaction of Ocean Waves and Wind*. Cambridge University Press.
- JANSSEN, P. A. E. M. & LIONELLO, P. 1989 On the interaction of wind and waves. *Phil. Trans. R. Soc. Lond. A* **329** (1604), 289–301.
- JEFFREYS, H. 1925 On the formation of water waves by wind. *Proc. R. Soc. Lond. A* **104**, 189–206.

- JESSUP, A. T. & ZAPPA, C. J. 1997 Defining and quantifying microscale wave braking with infrared imagery. *J. Geophys. Res.* **102** (C10) 23145–23153.
- KAWAI, S. 1979 Generation of initial wavelets by instability of a coupled shear flow and their evolution to wind waves. *J. Fluid Mech.* **93**, 661–703.
- KUDRYAVTSEV, V. N., MAKIN, V. K. & MEIRINK, J. F. 2001 Simplified model of the air flow above the waves. *Boundary-Layer Meteorol.* **100**, 63–90.
- LAMONT-SMITH, T. & WASEDA, T. 2008 Wind waves growth at short fetch. *J. Phys. Oceanogr.* **38**, 1597–1606.
- LARSON, T. R. & WRIGHT, J. W. 1974 Wind-generated gravity capillary waves: laboratory measurements of temporal growth rates using microwave backscatter. *J. Fluid Mech.* **70**, 417–436.
- LIBERZON, D. 2010 Experimental study of the initial stages of water waves generation by wind. PhD thesis, Tel Aviv University, Tel Aviv.
- LIBERZON, D. & SHEMER, L. 2010 An inexpensive method for measurements of static pressure fluctuations. *J. Atmos. Ocean. Technol.* **27** (4), 776–784.
- MAKIN, V. K. & KUDRYAVTSEV, V. N. 2002 Impact of dominant waves on sea drag. *Boundary-Layer Meteorol.* **103**, 83–99.
- MASTENBROEK, C., MAKIN, V. K., GARAT, M. H. & GIOVANANGELI, J. P. 1996 Experimental evidence of the rapid distortion of turbulence in the air flow over water waves. *J. Fluid Mech.* **318**, 273–302.
- MILES, J. W. 1957 On generation of surface waves by shear flows. *J. Fluid Mech.* **3**, 185–204.
- MILES, J. W. 1959 On generation of surface waves by shear flows. Part 2. *J. Fluid Mech.* **4**, 568–582.
- MILES, J. W. 1965 A note on the interaction between surface waves and wind profiles. *J. Fluid Mech.* **22**, 823–827.
- MILES, J. W. 1993 Surface wave generation revisited. *J. Fluid Mech.* **256**, 427–441.
- NISHIYAMA, R. T. & BEDARD, A. J. JR. 1991 A 'Quad-disk' static pressure probe for measurement in adverse atmospheres: With a comparative review of static pressure probe designs. *Rev. Sci. Instrum.* **62**, 2193–2204.
- PAPADIMITRAKIS, Y. A., HSU, E. Y. & STREET, R. L. 1986 The role of wave-induced pressure fluctuations in the transfer processes across an air–water interface. *J. Fluid Mech.* **170**, 113–137.
- PEIRSON, W. L. 1997 Measurement of surface velocities and shears at a wavy air–water interface using particle image velocimetry. *Exp. Fluids* **2**, 427–437.
- PEIRSON, W. L. & GARCIA, A. W. 2008 On the wind-induced growth of slow water waves of finite steepness. *J. Fluid Mech.* **608**, 243–274.
- PHILLIPS, O. M. 1957 On generation of waves by turbulent wind. *J. Fluid Mech.* **2**, 417–495.
- PLANT, W. J. 1982 A relationship between wind stress and wave slope. *J. Geophys. Res.* **87**, 1961–1967.
- PLANT, W. J. & WRIGHT, J. W. 1977 Growth and equilibrium of short gravity waves in a wind tank. *J. Fluid Mech.* **82**, 767–793.
- REUL, N., BRANGER, H. & GIOVANANGELI, J. P. 1999 Air flow separation over unsteady breaking waves. *Phys. Fluids* **11** (7), 1959–1961.
- REUL, N., BRANGER, H. & GIOVANANGELI, J. P. 2008 Air flow structure over short-gravity breaking water waves. *Boundary-Layer Meteorol.* **505**, 126–477.
- REUTOV, V. P. & TROITSKAYA, YU. I. 1996 Nonlinear effects due to water wave interactions with a turbulent wind. *Izv. Acad. Nauk SSSR Atmos. Ocean. Phys.* (English translation) **31** (6), 792–801.
- ROBERTSON, P. 1972 A direction-insensitive static head sensor. *J. Phys.* **E 5**, 1080–1082.
- SHAIKH, N. & SIDDIQUI, M. H. K. 2008 Airside velocity measurements over the wind-sheared water surface using particle image velocimetry. *Ocean Dyn.* **58**, 65–79.
- SHEMDIN, O. H. & HSU, E. Y. 1967 Direct measurement of aerodynamic pressure above a simple progressive gravity wave. *J. Fluid Mech.* **30**, 403–416.
- SHLICHTING, H. & GERSTEN, K. 2000 *Boundary Layer Theory*, 8th revised and enlarged edn. McGraw Hill.
- SIDDIQUI, M. H. K. & LOEWEN, M. R. 2007 Characteristics of the wind drift layer and microscale breaking waves. *J. Fluid Mech.* **573**, 417–456.

- SIDDIQUI, M. H. K. & LOEWEN, M. 2009 Phase-averaged flow properties beneath microscale breaking waves. *Boundary-Layer Meteorol.* **134**, 499–523.
- SIDDIQUI, M. H. K., LOEWEN, M. R., RICHARDSON, C., ASHER, W. E. & JESSUO, A. T. 2001 Simultaneous particle image velocimetry and infrared imagery of microscale breaking waves. *Phys. Fluids* **13** (7), 1891–1903.
- SNYDER, R. L. 1974 A field study of wave-induced pressure fluctuations above surface gravity waves. *J. Mar. Res.* **32**, 497–531.
- SNYDER, R. L., DOBSON, F. W., ELLIOT, J. A. & LONG, R. B. 1981 Array measurements of atmospheric pressure fluctuations above surface gravity waves. *J. Fluid Mech.* **102**, 1–59.
- STIASSNIE, M., AGNON, Y. & JANSSEN, P. A. M. 2007 Temporal and spatial growth of wind waves. *J. Phys. Oceanogr.* **37**, 106–114.
- SULLIVAN, P. P., MCWILLIAMS, J. C., & MOENG, C-H. 2000 Simulation of turbulent flow over idealized water waves. *J. Fluid Mech.* **404**, 47–85.
- THERRIEN, C. W. 1992 *Discrete Random Signals and Statistical Signal Processing*. Prentice Hall.
- TROITSKAYA, YU. I., SERGEEV, D. A., ERMAKOVA, O. S. & BALANDINA, G. N. 2010 Fine structure of the turbulent atmospheric boundary layer over the water surface. *Izv. Atmos. Ocean. Phys.* **46** (1), 109–120.
- UZ, B. M., HARA, T., BOCK, E. J. & DONELAN, M. 2003 Laboratory observations of gravity–capillary waves under transient wind forcing. *J. Geophys. Res.* **108** (C2), 3050–3080.
- VALENZUELA, G. R. 1976 The growth of gravity–capillary waves in a coupled shear flow. *J. Fluid Mech.* **76**, 229–250.
- VERON, F. & MELVILLE, W. K. 2001 Experiments on the stability and transition of wind-driven water surfaces. *J. Fluid Mech.* **446**, 25–65.
- VERON, F., SAXENA, G. & MISRA, S. 2007 Measurements of viscous tangential stresses in the separated airflow above wind waves. *Geophys. Res. Lett.* **34**, L19603.
- VERON, F., MELVILLE, W. K. & LENAIN, L. 2008 Wave-coherent air-sea heat flux. *J. Phys. Oceanogr.* **38**, 788–802.
- VERON, F., MELVILLE, W. K. & LENAIN, L. 2009 Measurements of ocean surface waves and surface turbulence interactions. *J. Phys. Oceanogr.* **39**, 2310–2323.
- WILCZAK, J. M. & BEDARD, A. J. 2004 A new turbulence microbarometer and its evaluation using the budget of horizontal heat flux. *J. Atmos. Ocean. Technol.* **21**, 1170–1181.
- WU, J. 1975 Wind-induced drift currents. *J. Fluid Mech.* **68**, 49–70.
- YOUNG, I. R. 1999 *Wind Generated Ocean Waves*. Elsevier.

Reproduced with permission of the copyright owner. Further reproduction prohibited without permission.